Report

Cell Reports

Nicotinic Cholinergic Receptors in VTA Glutamate Neurons Modulate Excitatory Transmission

Graphical Abstract

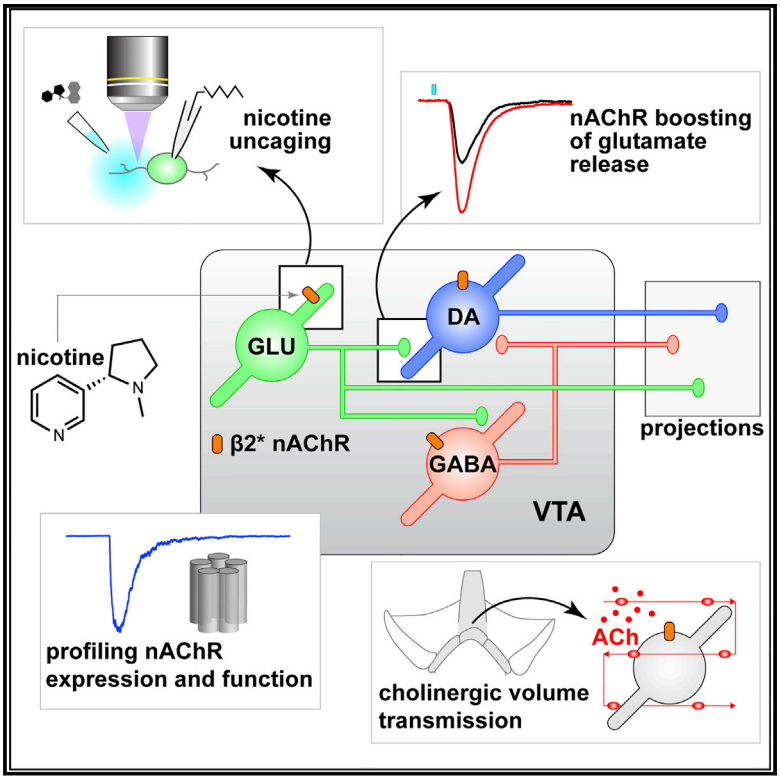

Authors

Yijin Yan, Can Peng, Matthew C. Arvin, ..., J. Michael McIntosh, Luke D. Lavis, Ryan M. Drenan

Correspondence

drenan@northwestern.edu

In Brief

Yan et al. examine how functional activity of nicotinic cholinergic receptors is distributed in diverse VTA cell types, revealing nAChR activity in VTA glutamate neurons. These receptors modulate local glutamate transmission in VTA, suggesting mechanisms by which nicotine influences mesolimbic circuitry.

Highlights

- VTA glutamate neurons are integrated into cholinergic circuits
- Functional heteromeric nAChRs are expressed in VTA glutamate neurons
- nAChRs modulate glutamate transmission in VTA microcircuits
- β2 nAChRs are required for nicotine modulation of glutamate transmission

Yan et al., 2018, Cell Reports *23*, 2236–2244
May 22, 2018
https://doi.org/10.1016/j.celrep.2018.04.062

CellPress

OPEN ACCESS
CellPress

Cell Reports
Report

Nicotinic Cholinergic Receptors in VTA Glutamate Neurons Modulate Excitatory Transmission

Yijin Yan,[1,6] Can Peng,[1,6] Matthew C. Arvin,[1,6] Xiao-Tao Jin,[1,6] Veronica J. Kim,[1] Matthew D. Ramsey,[1] Yong Wang,[1,5] Sambashiva Banala,[4] David L. Wokosin,[2] J. Michael McIntosh,[3] Luke D. Lavis,[4] and Ryan M. Drenan[1,7,*]

[1]Department of Pharmacology, Northwestern University Feinberg School of Medicine, Chicago, IL 60611, USA
[2]Department of Physiology, Northwestern University Feinberg School of Medicine, Chicago, IL 60611, USA
[3]George E. Wahlen Veterans Affairs Medical Center and Departments of Psychiatry and Biology, University of Utah, Salt Lake City, UT 84108, USA
[4]Janelia Research Campus, Howard Hughes Medical Institute, Ashburn, VA 20147, USA
[5]Present address: Virginia G. Piper Biodesign Center for Personalized Diagnostics, The Biodesign Institute, Arizona State University, Tempe, AZ 85287, USA
[6]These authors contributed equally
[7]Lead Contact
*Correspondence: drenan@northwestern.edu
https://doi.org/10.1016/j.celrep.2018.04.062

SUMMARY

Ventral tegmental area (VTA) glutamate neurons are important components of reward circuitry, but whether they are subject to cholinergic modulation is unknown. To study this, we used molecular, physiological, and photostimulation techniques to examine nicotinic acetylcholine receptors (nAChRs) in VTA glutamate neurons. Cells in the medial VTA, where glutamate neurons are enriched, are responsive to acetylcholine (ACh) released from cholinergic axons. VTA VGLUT2$^+$ neurons express mRNA and protein subunits known to comprise heteromeric nAChRs. Electrophysiology, coupled with two-photon microscopy and laser flash photolysis of photoactivatable nicotine, was used to demonstrate nAChR functional activity in the somatodendritic subcellular compartment of VTA VGLUT2$^+$ neurons. Finally, optogenetic isolation of intrinsic VTA glutamatergic microcircuits along with gene-editing techniques demonstrated that nicotine potently modulates excitatory transmission within the VTA via heteromeric nAChRs. These results indicate that VTA glutamate neurons are modulated by cholinergic mechanisms and participate in the cascade of physiological responses to nicotine exposure.

INTRODUCTION

Nicotine activates nicotinic acetylcholine receptors (nAChRs) in ventral tegmental area (VTA) neurons, which depolarizes the membrane potential, enhances firing, and boosts dopamine (DA) release in target structures such as nucleus accumbens (NAc) (Brazell et al., 1990; Calabresi et al., 1989). VTA DAergic and GABAergic neurons strongly express nAChRs, and nicotine acts on VTA circuitry by (1) stimulating DA neurons via nAChR activation (Calabresi et al., 1989), (2) inhibiting such neurons through nAChR activation on VTA GABA neurons (Mansvelder et al., 2002), and (3) facilitating glutamate release from afferents expressing α7 nAChRs (Mansvelder and McGehee, 2000). This framework has been valuable, but recent appreciation for VTA glutamate neurons indicate that it is incomplete. These cells are enriched in the medial VTA (mVTA) and project to several forebrain structures (Hnasko et al., 2012; Ntamati and Lüscher, 2016; Qi et al., 2016; Root et al., 2014a, 2014b; Yoo et al., 2016). These circuits are functionally significant, being involved in both reward and aversion (Qi et al., 2016; Root et al., 2014a; Yamaguchi et al., 2007; Yoo et al., 2016). VTA glutamate neurons also make widespread intrinsic contacts with DAergic and non-DAergic neurons within the VTA itself (Dobi et al., 2010; Wang et al., 2015; Yoo et al., 2016).

Glutamatergic transmission in the VTA plays a critical role in nicotine dependence (Kenny et al., 2009), but the receptor and circuitry mechanisms are unclear. Whether and how nicotine modulates VTA output by impinging on intrinsic glutamatergic circuitry in VTA is completely unknown. On the basis of the influence of these neurons on local VTA circuitry, their distinct connectivity pattern with target structures, and their ability to co-release DA or GABA (Stamatakis et al., 2013; Stuber et al., 2010), we speculated that if nAChRs are functionally expressed in VTA glutamate neurons, they could be uniquely positioned to influence motivated behavior circuits by enhancing excitatory transmission within, and downstream of, the VTA. In this study, we demonstrate the existence of functional nAChRs in VTA glutamate neurons, characterize their pharmacological properties, examine their subcellular distribution pattern, and uncover a role for them in intrinsic excitatory transmission in VTA microcircuits.

RESULTS

nAChRs Are Expressed in mVTA Neurons

During patch-clamp recordings and two-photon laser scanning microscopy (2PLSM) imaging of dye-filled mVTA neurons in slices from mice expressing tdTomato (tdT) in cholinergic

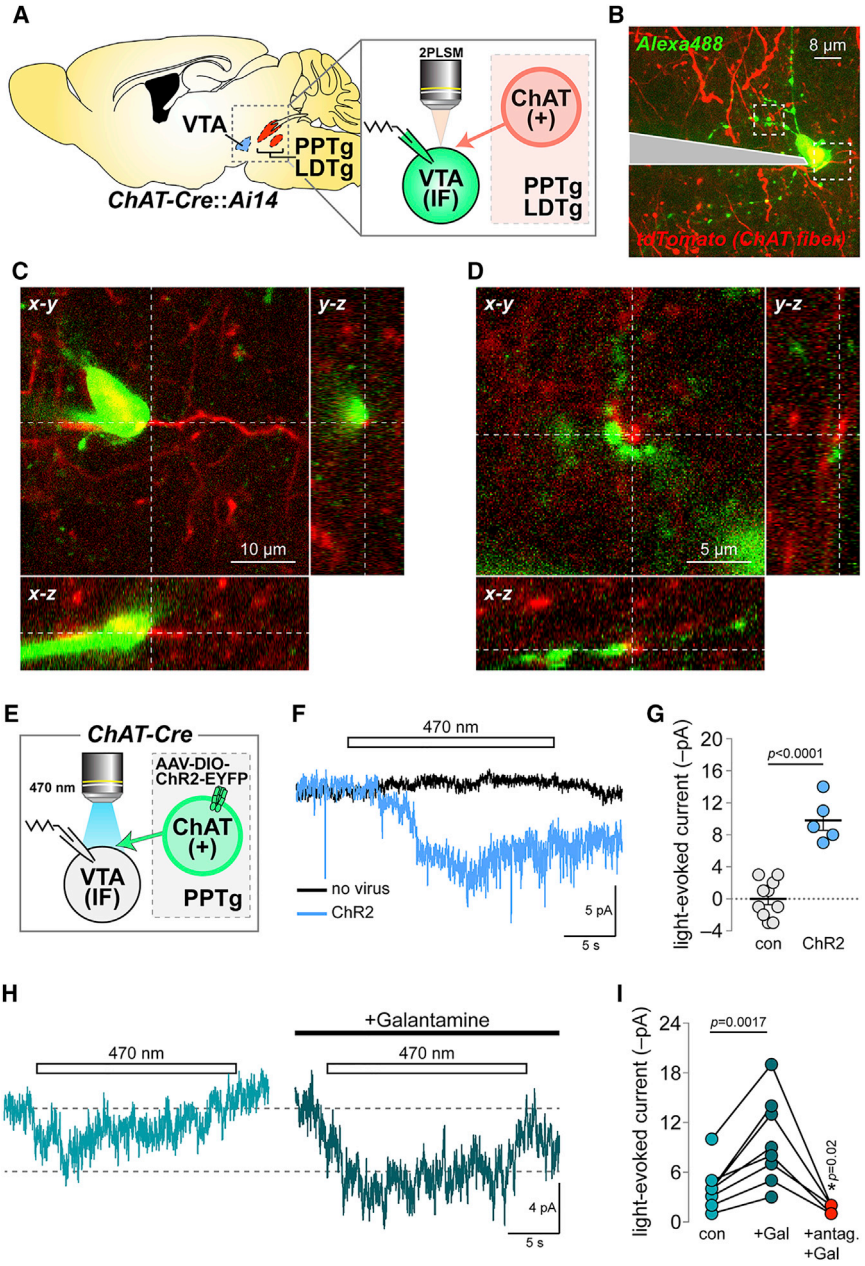

Figure 1. Medial VTA nAChRs Participate in Cholinergic Transmission

(A) Imaging and recording configuration for (B)–(D).

(B) 2PLSM image of a dye-filled mVTA neuron and cholinergic fibers.

(C and D) Soma (C) and dendrites (D) from the cell in (B) shown proximal to cholinergic fibers. Representative of n = 4 cells/n = 3 mice.

(E) Approach used in (F)–(I).

(F) Voltage clamp current deflections during 470 nm light flashes (20 s) in slices from $ChR2^-$ versus $ChR2^+$ mice. Averaged traces for five to ten cells shown.

(G) Light-evoked current amplitudes for (n = 9/2 and n = 5/2) neurons in control (no virus) and $ChR2^+$ mice. (scatter plot with mean ± SEM). p value is from a two-sided unpaired t test.

(H) Averaged photocurrents (470 nm, 20 s flash) for neurons from $ChR2^+$ mice ± galantamine (1 μM).

(I) Light-evoked current amplitudes for (n = 8/4) individual neurons before drug (con), during galantamine (Gal) application, and during co-application of galantamine + nAChR antagonist cocktail (10 μM DHβE, 100 nM α-Ctx MII, 10 nM MLA). p values are from two-sided paired t tests.

See also Figure S1.

somata/axons (ChAT-Cre::Ai14 mice) (Figure 1A), we noted a modest number of tdT^+ fibers adjacent to mVTA neurons (Figure 1B). Analysis of image stacks in x-y, y-z, and x-z planes revealed cholinergic fibers in close apposition to neuronal somata and dendrites (Figures 1C and 1D), suggesting that these neurons are sensitive to ACh. This is supported by results localizing α4, α6, β2, and β3 nAChR subunits to mVTA neurons of knockin mice expressing GFP-fused nAChRs (Shih et al., 2014) (Figures S1A and S1B). To examine ACh sensitivity of mVTA cells, ChR2-EYFP was expressed and functionally validated in pedunculopontine tegmental nucleus (PPTg) cholinergic neurons of ChAT-Cre mice (Figures 1E and S1C–S1H). Voltage-clamped mVTA neurons in slices containing $ChR2\text{-}EYFP^+$ fibers were photostimulated with 470 nm light flashes (20 s, 0.12 mW/mm^2), producing a slow inward current (Figures 1F and 1G). Galantamine (1 μM; validated in Figures S1I and S1J) enhanced these photocurrents (Figures 1H and 1I), whereas co-application of a nAChR antagonist cocktail with galantamine eliminated them (Figure 1I). Following Cre-independent expression of ChR2-EYFP in PPTg of ChAT-Cre mice, we recorded fast glutamatergic optically evoked excitatory postsynaptic currents (oEPSCs) in mVTA neurons (Figures S1K–S1M). This reflects underlying differences in neurotransmission between cholinergic versus non-cholinergic PPTg fibers to mVTA neurons. Collectively, these results indicate that mVTA neurons participate in cholinergic transmission through nAChRs.

mVTA Glutamate Neurons Express Functional nAChRs

To examine nAChR subunit expression in VTA glutamate neurons, triple-channel mRNA fluorescence *in situ* hybridization (FISH) was used. First, nAChR probes (*Chrna4*, *Chrna6*, and *Chrnb2*) were validated (Figures S2A–S2I). Co-labeling of mVTA interfascicular nucleus (IF) neurons with probes for *Slc17a6* (VGLUT2), *Chrna4*, and *Th* revealed multiple co-expression patterns (Figure 2A), indicating that a majority of $Slc17a6^+$ neurons are positive for *Chrna4* (Table S1; Figures 2B and 2C).

Within *Slc17a6*$^+$/*Chrna4*$^+$ neurons, a majority also express *Th* (Table S1; Figure 2C). Co-labeling of *Slc17a6* and *Chrna4* was qualitatively similar in lateral VTA neurons, as was the fraction of *Slc17a6*$^+$/*Chrna4*$^+$ neurons that co-labeled for *Th* (Table S1; Figures 2D and 2E). The same analysis using probes for *Chrna6* and *Chrnb2* produced very similar results (Figures 2F–2O). To determine whether the nAChR expression profile in VTA glutamate neurons is unique or generalizable, we examined nAChR expression in GABA (*Gad2*$^+$) neurons with FISH (Figures S2J, S2O, and S2T). Like *Slc17a6* labeling revealed, a majority of IF *Gad2*$^+$ cells express *Chrna4*, *Chrna6*, and *Chrnb2* (Figures S2K, S2L, S2P, S2Q, S2U, and S2V). Interestingly, *Th* was expressed in 30%–50% of *Gad2*$^+$/nAChR$^+$ neurons, depending on the subunit examined (Figures S2L, S2Q, and S2V). Compared with mVTA IF, lateral VTA neurons tend to have fewer neurons co-labeling for *Gad2* and nAChR subunits as well as fewer *Th*$^+$ neurons that co-labeled for *Gad2* and nAChR subunits (Figures S2M, S2N, S2R, S2S, S2W, and S2X).

To fluorescently mark mVTA glutamate neurons in adult mice for analysis of functional nAChRs, hM4Gi-mCherry (DREADD receptor) was expressed in mVTA of VGLUT2-Cre mice (Figures 3A and S3A). Robust ACh-elicited currents were recorded in VGLUT2$^+$ IF neurons (Figure 3B), and pharmacological analysis indicated that $\alpha6\beta2$ and $\alpha4\beta2$(non-$\alpha6$) were the dominant nAChR subtypes (Figure 3C). To compare these currents with those in VTA GABA and DA neurons, GAD2-Cre and DAT-Cre mice, respectively, were crossed with mice (Ai14 strain) driving tdT expression in a Cre-dependent manner (Figures 3D and 3G). Relative to results in VGLUT2$^+$ neurons (Figures 3B and 3C), ACh-evoked currents in VTA GABA (Figures 3E and 3F) and DA (Figures 3H and 3I) neurons were qualitatively similar. Presynaptic blockers partially reduced the currents in VTA VGLUT2$^+$ neurons (Figure 3J), but a vehicle control experiment demonstrated that run-down of nAChR currents cannot account for the reduction in current we observed during pharmacological analysis (Figure 3K). To control for strain differences in nAChR function, we performed a similar analysis in unlabeled VTA IF neurons from C57BL/6 mice. These results from a presumptive pool of DA/GABA/VGLUT2 neurons were similar to results in the Cre lines (Figures S3B and S3C). In pooled C57BL/6 but not VGLUT2$^+$, GAD2$^+$, or DAT$^+$ VTA neurons (two-sided paired t tests, respectively: $p = 0.0283$, $p = 0.1136$, $p = 0.0860$, and $p = 0.1327$), an $\alpha7$ nAChR antagonist (methyllycaconitine [MLA]; 10 nM) further reduced the residual ACh-evoked current that was insensitive to combined α-Ctx MII[H9A;L15A]+DHβE treatment.

Next, we asked whether nAChRs in mVTA glutamate neurons are localized to somata or dendrites. VGLUT2$^+$ IF neurons in slices from VGLUT2-Cre::AAV-DIO-hM4Gi-mCherry mice were identified via tdT fluorescence using 2PLSM imaging (Figure 3A). Photoactivatable nicotine (PA-Nic) (Banala et al., 2018) (Figure 3L) was used to study functional nAChR responses in mVTA VGLUT2$^+$ neurons during recording and 2PLSM imaging. PA-Nic photolysis (405 nm, 2 mW) in spots (1 μm diameter) adjacent to VGLUT2$^+$ neuron somata and dendrites revealed fast inward currents (Figure 3M), indicating the presence of functional somatodendritic nAChRs in mVTA glutamate neurons.

mVTA Glutamate Neuron nAChRs Modulate Excitatory Neurotransmission

To determine whether nAChRs modulate glutamatergic transmission between VTA glutamate and non-glutamate neurons, we first validated Cre-dependent ChR2 expression in VGLUT2-Cre mice by microinjecting AAV-DIO-ChR2-EYFP into mVTA of VGLUT2-Cre::Ai14 mice. These microinjections largely saturated the mVTA with ChR2$^+$ fibers and infected VGLUT2$^+$ cell bodies (Figure 4A). Next, we recorded from local uninfected neurons in mVTA to study excitatory transmission between ChR2$^-$ (putative VGLUT2$^-$) and ChR2$^+$ (VGLUT2$^+$) neurons (Figure 4B, left). Full-field illumination (470 nm, 1–5 ms) activated ChR2 on VGLUT2$^+$ somata and local terminals, evoking oEPSCs in ChR2$^-$ mVTA neurons (Figure 4B, right) that were sensitive to NBQX + D-AP5. oEPSCs in ChR2$^-$ neurons were distinguishable from direct photocurrents in VGLUT2$^+$ neurons via their clear synaptic delay and faster decay time constant (Figure 4C). To examine whether nAChRs in VGLUT2$^+$ mVTA neurons modulate these oEPSCs, we compared the oEPSC amplitude ± nicotine (0.3 μM). Nicotine application enhanced oEPSC amplitude in mVTA ChR2$^-$ neurons (Figures 4D and 4E), demonstrating a role for nAChRs in excitatory transmission between mVTA VGLUT2$^+$ and ChR2$^-$ (putative VGLUT2$^-$) neurons. Nicotine (0.3 μM) was unable to enhance oEPSC amplitudes in the presence of DHβE (repeated-measures [RM] one-way ANOVA of ACSF versus ACSF + DHβE versus ACSF + DHβE + nicotine; $F[1.577, 7.885] = 1.523$, $p = 0.2698$) (Figure 4F), implicating $\beta2$-containing nAChRs.

To determine whether nicotine acts directly or indirectly to influence oEPSCs, we knocked down $\beta2$ nAChR subunits selectively in VGLUT2$^+$ mVTA neurons using CRISPR/Cas9. VGLUT2-Cre mice crossed to Rosa26-LSL-Cas9-2A-EGFP mice (referred to as R26-LSL-Cas9) were microinjected in mVTA with adeno-associated virus (AAV) vectors delivering single guide RNAs (sgRNAs) targeting *Chrnb2* or no specific gene (control) (Figure 4G). Comparison of 1 mM ACh-evoked current amplitudes in R26-LSL-Cas9::VGLUT2-Cre mice expressing control or *Chrnb2*-targeted sgRNAs confirmed functional knockdown of nAChRs (Figures 4H and 4I). As an additional control for *Chrnb2* knockdown, nicotine (0.3 μM) increased cell-attached firing in VGLUT2$^+$ mVTA neurons from mice expressing control sgRNAs but not *Chrnb2* sgRNAs (Figures 4J and 4K). To study the effect of *Chrnb2* knockdown on nAChR-modulated oEPSCs between VGLUT2$^+$ and ChR2$^-$ mVTA neurons, ChR2-EYFP was expressed in VGLUT2$^+$ neurons of control or *Chrnb2* knockdown mice. Whereas nicotine could still enhance oEPSCs in ChR2$^-$ mVTA neurons from control sgRNA-injected mice, oEPSC enhancement by nicotine was blocked in *Chrnb2* sgRNA-injected mice (RM two-way ANOVA: control/*Chrnb2* virus [$F(1, 8) = 0.8818$, $p = 0.3752$] × drug treatment [$F(1, 8) = 9.193$, $p = 0.0163$], interaction [$F(1, 8) = 40.27$, $p = 0.0002$]) (Figures 4L and 4M).

Last, we asked whether presynaptic nAChRs on glutamatergic fibers in NAc from VTA VGLUT2$^+$ neurons modulate glutamate transmission onto NAc neurons. ChR2-EYFP expression in NAc medial shell following mVTA microinjection of AAV-DIO-ChR2-EYFP was first validated (Figure S4A). Although excitatory oEPSCs were evident (Figure S4B, left), nicotine (0.3 μM) did not

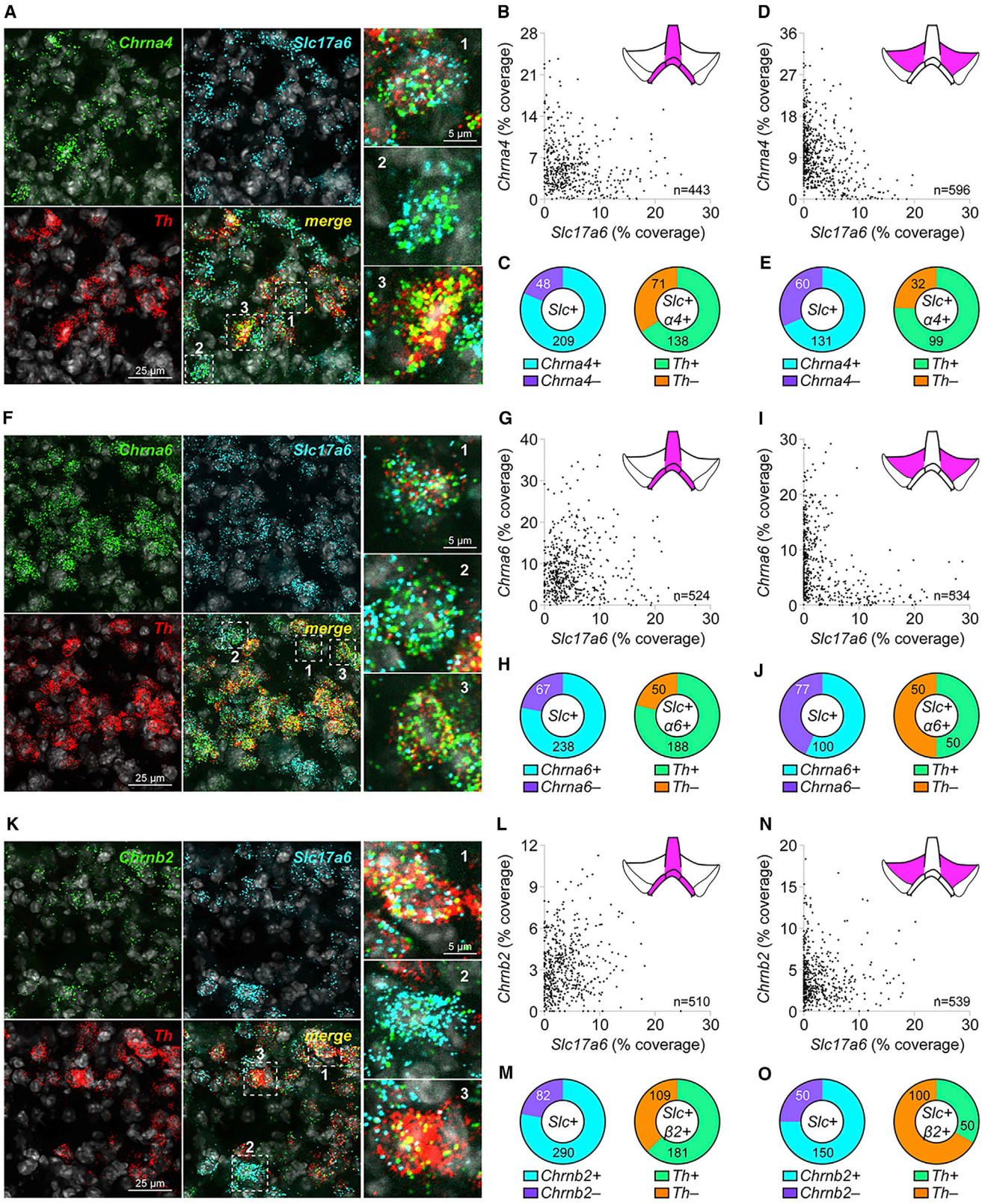
A
Chrna4
Slc17a6
Th
merge
25 μm
5 μm
B
Chrna4 (% coverage)
Slc17a6 (% coverage)
n=443
C
Slc+
209
48
Chrna4+
Chrna4–
Slc+ α4+
138
71
Th+
Th–
D
n=596
E
131
60
99
32
F
Chrna6
G
n=524
H
238
67
188
50
I
n=534
J
100
77
50
K
Chrnb2
L
n=510
M
290
82
Slc+ β2+
181
109
N
n=539
O
150
50
100
(legend on next page)

boost these responses (Figure S4B, right). To control for functional nAChRs in the mVTA to NAc projection, fluorescent retrograde tracers were used. After confirming that NAc medial shell microinjection of green retrobeads efficiently labels mVTA neurons (Figure S4C), we labeled NAc medial shell-projecting VGLUT2$^+$ mVTA neurons by microinjecting green retrobeads into NAc medial shell of VGLUT2-Cre::Ai14 mice (Figure S4D). Such neurons were visually identified in the slice via dual red (tdT$^+$)/green (retrobead$^+$) fluorescence. ACh-evoked currents were evident in these cells (Figures S4E and S4F), confirming functional nAChR expression in VTA to NAc VGLUT2$^+$ cells. These results rule out the interpretation that nicotine failed to modulate NAc glutamate transmission because of a lack of nAChR expression. Nicotine-modulated oEPSCs (Figures 4D and 4E) may occur in mVTA DAT$^+$ and/or GAD2$^+$ neurons, but these neuron types were not uniquely identifiable when examining I_h current amplitude, action potential firing rate, or input resistance (Figures S4G–S4J).

DISCUSSION

In this study, we examined how nAChR distribution and function maps onto the trio (DAT, GAD2, VGLUT2) of neurotransmitter-defined VTA neurons by examining these receptors in glutamate neurons and comparing their expression and function with nAChRs in DA and GABA neurons. β2-containing nAChRs, which exhibit high sensitivity to ligand and strong nicotine-mediated desensitization (Pidoplichko et al., 1997), are the predominant subtype in VTA glutamate neurons. This is consistent with prior work (Klink et al., 2001) but extends those findings by suggesting not only nicotinic cholinergic modulation of glutamate release from VTA neurons but similar modulation of DA/glutamate (Stuber et al., 2010) and GABA/glutamate (Root et al., 2014b; Yoo et al., 2016) co-release. Given that VTA VGLUT2$^+$ neurons project to atypical forebrain targets, cholinergic modulation of VTA-derived glutamatergic afferents may occur at synapses that are not yet characterized. Consistent with the relatively non-specific targeting of VTA DAT/GAD2/VGLUT2 neurons by hindbrain cholinergic nuclei (Faget et al., 2016), we did not find evidence for selective expression of particular nAChR subtypes in VTA glutamate neurons. However, individual VGLUT2$^+$, DAT$^+$, and GAD2$^+$ cells express different levels of functional nAChR subtypes (Figure 3).

Our results showing innervation of mVTA neurons by cholinergic fibers extend prior work in ChAT-Cre rats (Dautan et al., 2016; Xiao et al., 2016). 2PLSM imaging (Figures 1B–1D) and optogenetic data (Figure S1H) show modest to sparse innervation of IF neurons by cholinergic fibers. This is consistent with slow kinetics of inward currents activated by optical release of ACh (Figures 1F and 1H). Prolonged photostimulations (20 s) were required to elicit these currents, and we found no evidence for fast (millisecond timescale) cholinergic transmission. On this basis, volume transmission may be the operable cholinergic mechanism in mVTA. Despite this likelihood, we also uncovered fast (millisecond timescale) nAChR currents at VTA VGLUT2$^+$ neuronal somata and dendrites when rapidly "jumping" the concentration of exogenous nicotine using laser photolysis of PA-Nic (Figure 3M). This strongly suggests that slow responses following optical release of ACh reflect intrinsic limitations imposed by cholinergic transmission rather than receptor activation/desensitization kinetics. Nicotine photolysis confirms what has previously only been inferred: VTA nAChRs are not only located on somata where they likely modulate firing, but also in dendrites where they may mediate cholinergic modulation of dendritic integration. Last, nicotine photolysis studies, juxtaposed with optical release of ACh, illustrate the dramatic difference between endogenous ACh transmission and how it is biophysically "highjacked" by nicotine.

A local glutamatergic connection in VTA between VGLUT2$^+$ and TH$^+$ neurons has been described that modulates reward processing (Wang et al., 2015; Yoo et al., 2016). The present work extends those results by revealing that nicotine can potently enhance excitatory transmission at these synapses. In doing so, nicotine increases the gain and reliability of local glutamate to DA neuron transmission. Additionally, by this activity, nicotine will likely sensitize mVTA DA and/or GABA neurons to other excitatory input, such as corticolimbic glutamate

Figure 2. VTA Glutamate Neurons Express Heteromeric nAChRs

(A–E) Co-expression of (mRNA) *Chrna4* and (mRNA) *Slc17a6* in VTA neurons.

(A) Fluorescence *in situ* hybridization (FISH) in mVTA neurons for probes: *Chrna4*, *Slc17a6* (VGLUT2), and *Th*. *Chrna4*$^+$ neurons indicated in "merge" panel and shown enlarged (right), were (1) *Chrna4*$^+$/*Slc17a6*$^+$/*Th*$^+$, (2) *Chrna4*$^+$/*Slc17a6*$^+$/*Th*$^-$, and (3) *Chrna4*$^+$/*Slc17a6*$^-$/*Th*$^+$.

(B) Scatterplot of *Slc17a6* (abscissa) and *Chrna4* (ordinate) "% coverage" for all analyzed neurons.

(C) Left: pie graph of *Slc17a6*$^+$ neurons that were *Chrna4*$^+$ versus *Chrna4*$^-$. Right: *Th* expression for *Slc17a6*$^+$/*Chrna4*$^+$ neurons from left pie graph.

(D and E) *Chrna4*/*Slc17a6* co-expression in lateral VTA was performed as in mVTA (B and C).

(F–J) Co-expression of (mRNA) *Chrna6* and (mRNA) *Slc17a6* in VTA neurons.

(F) Fluorescence *in situ* hybridization (FISH) in mVTA neurons for probes: *Chrna6*, *Slc17a6* (VGLUT2), and *Th*. *Chrna6*+ neurons indicated in 'merge' panel, and shown enlarged (right panels), were: 1) *Chrna6*+/*Slc17a6*+/*Th*+; 2) *Chrna6*+/*Slc17a6*+/*Th*−; 3) *Chrna6*+/*Slc17a6*−/*Th*+.

(G) Scatter plot of *Slc17a6* (abscissa) and *Chrna6* (ordinate) '% coverage' for all analyzed neurons.

(H) Left: Pie graph of *Slc17a6*+ neurons that were *Chrna6*+ vs. *Chrna6*−. Right: *Th* expression for *Slc17a6*+/*Chrna6*+ neurons from left pie graph.

(I and J) *Chrna6*/*Slc17a6* co-expression in lateral VTA was performed as in mVTA (G and H).

(K–O) Co-expression of (mRNA) *Chrnb2* and (mRNA) *Slc17a6* in VTA neurons.

(K) Fluorescence *in situ* hybridization (FISH) in mVTA neurons for probes: *Chrnb2*, *Slc17a6* (VGLUT2), and *Th*. *Chrnb2*+ neurons indicated in 'merge' panel, and shown enlarged (right panels), were: 1) *Chrnb2*+/*Slc17a6*+/*Th*+; 2) *Chrnb2*+/*Slc17a6*+/*Th*−; 3) *Chrnb2*+/*Slc17a6*−/*Th*+.

(L) Scatter plot of *Slc17a6* (abscissa) and *Chrnb2* (ordinate) '% coverage' for all analyzed neurons.

(M) Left: Pie graph of *Slc17a6*+ neurons that were *Chrnb2*+ vs. *Chrnb2*−. Right: *Th* expression for *Slc17a6*+/*Chrnb2*+ neurons from left pie graph.

(N and O) *Chrnb2*/*Slc17a6* co-expression in lateral VTA was performed as in mVTA (L and M).

Complete data for nAChR/*Slc17a6* FISH are listed in Table S1. Data are pooled from n = 3 mice. See also Figure S2 and Table S2.

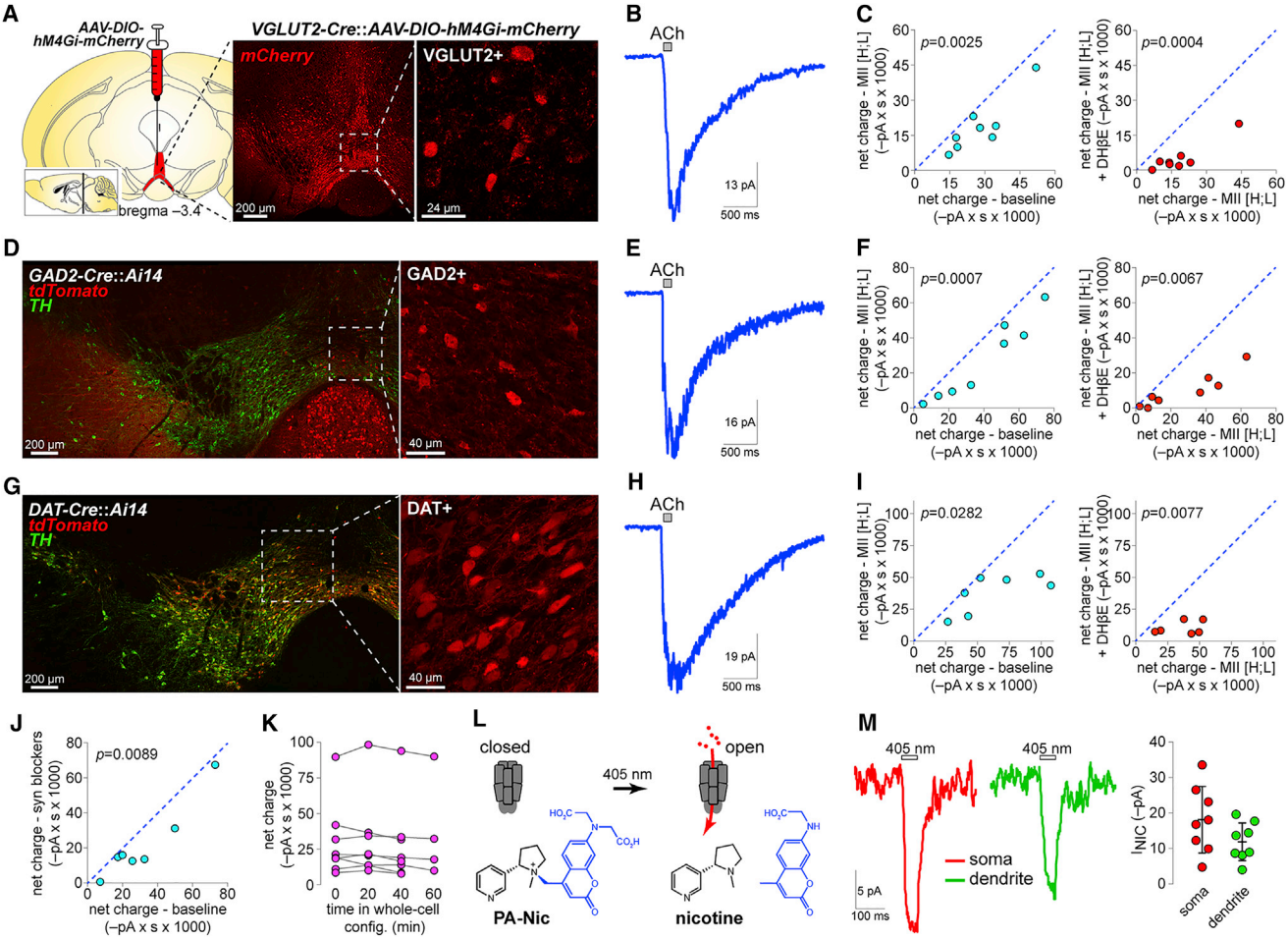

Figure 3. Functional nAChRs in VTA Glutamate Neurons

(A) hM4Gi-mCherry vectors were unilaterally microinjected in mVTA of VGLUT2-Cre mice, and DsRed stain (middle) shows infected neurons. Right 2PLSM image shows hM4Gi-mCherry in VGLUT2$^+$ neurons of acute slices.

(B) Averaged trace for application of 1 mM ACh to VGLUT2$^+$ mVTA neurons.

(C) Left: 1 mM ACh-induced net charge ± α-Ctx MII[H9A;L15A] for (n = 8 cells/n = 3 mice) VGLUT2$^+$ neurons. Right: 1 mM ACh-induced net charge in the presence of α-Ctx MII[H9A;L15A] versus α-Ctx MII[H9A;L15A] + 1 μM DHβE for the same neurons shown at left. p values are from two-sided paired t tests.

(D and G) DsRed/TH stain for GAD2-Cre::Ai14 and DAT-Cre::Ai14 (D, left). tdTomato channel (G, left) shows GAD2$^+$ (D, right) and DAT$^+$ (G, right) neurons targeted for recordings.

(E, F, H, and I) Averaged 1 mM ACh-evoked responses (E and H) and pharmacological analysis (F and I), conducted as described in (B) and (C), are shown for GAD2$^+$ (n = 8/2) and DAT$^+$ (n = 7/2) neurons, respectively.

(J) ACh (1 mM)-induced net charge ± [CNQX (10 μM), D-AP5 (50 μM), TTX (0.5 μM), picrotoxin (100 μM)]. n = 7/2 VGLUT2$^+$ neurons. p value is from a two-sided paired t test.

(K) Net charge responses to repeated application of 1 mM ACh for n = 8/2 mVTA VGLUT2$^+$ neurons. Vehicle (ACSF) was superfused and responses recorded at indicated times after break-in.

(L) Photoactivatable nicotine (PA-Nic) was applied to neurons, and nicotine was uncaged with focal 405 nm laser photolysis.

(M) Representative voltage clamp PA-Nic photolysis responses (traces) and summary plot (right; mean ± SD) for perisomatic and dendritic uncaging locations in mVTA VGLUT2$^+$ neurons (n = 8/2).

See also Figure S3.

transmission (Mansvelder and McGehee, 2000) and direct nAChR stimulation by nicotine or ACh. Although presynaptic nAChRs are abundant in DA axons of dorsal striatum and NAc (Champtiaux et al., 2002), nicotine did not modulate VTA to NAc glutamate transmission (Figures S4A–S4F). Future work will be required to determine whether nAChRs in VTA VGLUT2$^+$ neurons are specifically targeted to DA-releasing axonal compartments (Zhang et al., 2015) or are excluded from presynaptic compartments altogether.

Nicotine's reinforcing property is critically dependent on its interaction with VTA circuitry. Until now, the totality of nicotine's action in VTA was assumed to involve activation of nAChRs on DA and GABA neurons coupled with potentiation of glutamatergic and GABAergic afferents (Champtiaux et al., 2002; Klink

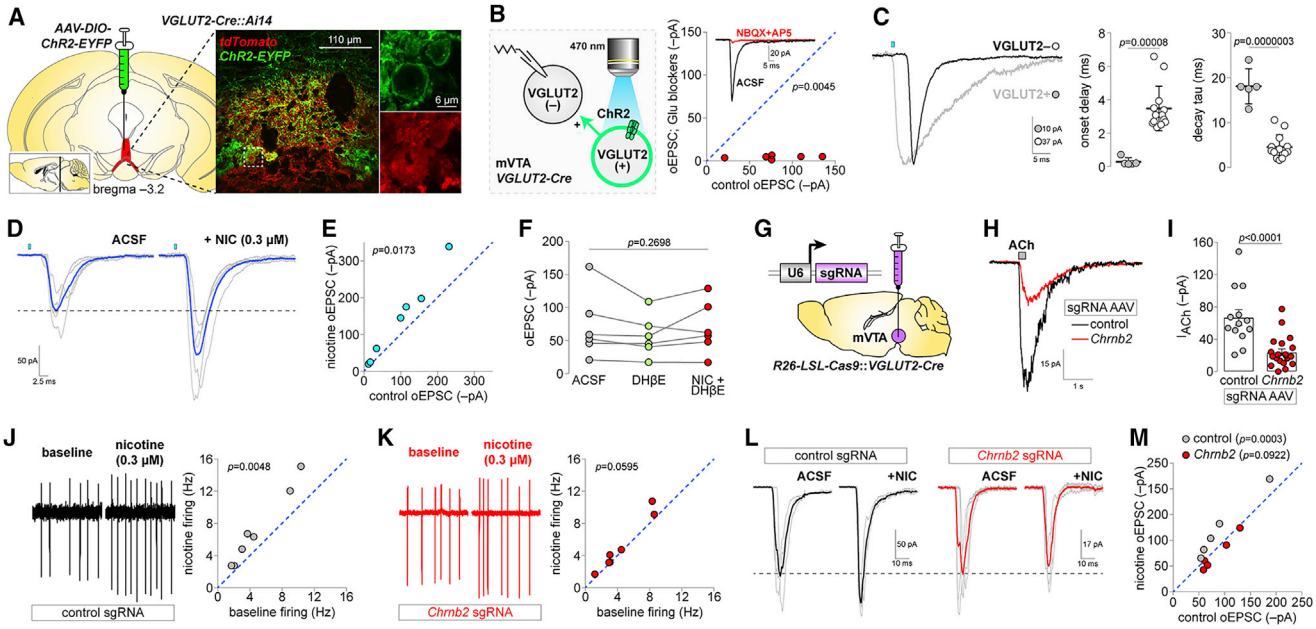

Figure 4. nAChRs in mVTA Glutamate Neurons Modulate Excitatory Transmission

(A) ChR2-EYFP vectors were unilaterally microinjected in mVTA of VGLUT2-Cre::Ai14 mice and sections stained for DsRed/GFP (large image). Enlarged views (right) of boxed area show VGLUT2$^+$ neuron expression of ChR2-EYFP.

(B) In mVTA slices from VGLUT2-Cre mice microinjected as described in (A), oEPSCs were recorded in ChR2$^-$ neurons (left). oEPSCs sensitivity to NBQX (10 μM)+D-AP5 (50 μM) (right; n = 6 cells/n = 3 mice). p value is from a two-sided paired t test.

(C) Representative oEPSC and photocurrent in ChR2$^-$ and ChR2$^+$/VGLUT2$^+$ neuron, respectively (left). Photocurrent and oEPSC onset delay and decay tau in (n = 5/4) ChR2$^+$/VGLUT2$^+$ and (n = 13/9) ChR2$^-$ mVTA neurons (scatterplots; mean ± SD). p values are from two-sided unpaired t tests.

(D) Representative oEPSC (individual trials, gray; averaged trace, blue) for ChR2$^-$ neurons ± nicotine (0.3 μM).

(E) Control versus nicotine-enhanced oEPSC current amplitude (n = 7/5). p values are from two-sided paired t tests.

(F) oEPSC amplitude in ChR2$^-$ neurons (n = 6/6) during bath application of ACSF (control), ACSF+DHβE (1 μM), and ACSF+DHβE (1 μM)+nicotine (0.3 μM). p value is from repeated-measures one-way ANOVA.

(G) CRISPR/Cas9 knockdown approach. R26-LSL-Cas9::VGLUT2-Cre mice were microinjected in mVTA with sgRNA AAVs.

(H–K) Validation of *Chrnb2* knockdown. ACh (1 mM)-evoked currents (H, representative traces; I, summary scatterplot with mean ± SEM) in VGLUT2$^+$ neurons from R26-LSL-Cas9::VGLUT2-Cre mice microinjected in mVTA with control (n = 14/4) or *Chrnb2* (n = 21/6) sgRNA AAVs. Cell-attached firing ± nicotine (0.3 μM) in VGLUT2$^+$ neurons from R26-LSL-Cas9::VGLUT2-Cre mice microinjected in mVTA with (J) control (n = 7/5) or (K) *Chrnb2* (n = 7/6) sgRNA AAVs. p values are from two-sided paired t tests.

(L and M) Effect of *Chrnb2* knockdown on nicotine-enhanced glutamate transmission in VTA. R26-LSL-Cas9::VGLUT2-Cre mice prepared as shown in (G) were microinjected in mVTA with AAV-DIO-ChR2-EYFP and oEPSCs in ChR2$^-$ cells recorded. Representative oEPSC traces (L) (individual trials, gray; averaged trace, black/red) and summary data (M) for nicotine (0.3 μM)-mediated changes in oEPSC amplitude are shown for control (n = 5/3) and *Chrnb2* (n = 5/4) knockdown. p values are from Sidak's multiple-comparisons test after two-way repeated-measures ANOVA.

See also Figure S4.

et al., 2001; Mansvelder et al., 2002; Mansvelder and McGehee, 2000). Our demonstration that nAChRs on VTA glutamate neurons modulate local microcircuits adds an additional level of complexity to our understanding of nicotine's action in mesolimbic circuits. These results require that we update the existing framework regarding nicotine-elicited modulation of electrical and chemical signaling in the mesocorticolimbic system.

EXPERIMENTAL PROCEDURES

Mice

All experimental protocols involving mice were approved by the Institutional Animal Care and Use Committee at Northwestern University (protocols IS00003282, IS00003604, and IS00006642). Procedures also followed the guidelines for the care and use of animals provided by the NIH Office of Laboratory Animal Welfare. All efforts were made to minimize distress and suffering during experimental procedures, including during the use of anesthesia. Mice were housed at 22°C on a 12 hr light/dark cycle with food and water *ad libitum*. Mice were weaned on postnatal day 21 and housed with same-sex littermates. A tail sample was taken from each mouse for genotyping via PCR as previously described (Drenan et al., 2008). Creation and characterization of knockin (α3-GFP, α4-GFP, β2-GFP, β3-GFP, and β4-GFP) or bacterial artificial chromosome transgenic mice (α6-GFP) harboring in-frame insertions of GFP into the coding sequence of specific nAChR subunit genes have been previously described (Mackey et al., 2012; Shih et al., 2014). The following mouse strains were obtained from The Jackson Laboratory: ChAT-IRES-Cre (Jax 006410), VGLUT2-IRES-Cre (Jax 016963), DAT-IRES-Cre (Jax 06660), GAD2-IRES-Cre (Jax 010802), Rosa26-LSL-Cas9-2A-EGFP (Jax 026175), Ai14 (Jax 007908), and C57BL/6J (Jax 000664). Mice expressing tdT in a Cre-dependent manner (ChAT-IRES-Cre::Ai14, VGLUT2-IRES-Cre::Ai14, GAD2-IRES-Cre::Ai14, and DAT-IRES-Cre::Ai14) or Cas9 in a Cre-dependent manner (R26-LSL-Cas9::VGLUT2-Cre) were obtained by crossing mice heterozygous for each mutation, which

produced ~25% double-heterozygous progeny. Male and female mice (aged 6–24 weeks) were used in approximately equal numbers.

mRNA Expression Analysis

In brief, mRNA expression was performed by hybridizing probes targeting genes of interest to brain tissue sections. All probes were acquired from Advanced Cell Diagnostics (ACD). Procedures were conducted as described in the ACD RNAscope Fluorescent Multiplex Assay manual. Confocal images of probe-labeled sections were analyzed using ImageJ (NIH) to identify cells expressing each probe target. A full description of our analysis routine, which was adapted from (Wallace et al., 2017), is provided in the Supplemental Information.

Electrophysiological Recordings

Brain slices were prepared from adult (>6 weeks) mice as previously described (Engle et al., 2012). Neurons were visualized using a Scientifica Slicescope or a Nikon Eclipse FN-1, and fluorescent markers (tdT, mCherry, EYFP, etc.) were used to make targeted recordings. Whole-cell recordings were made using glass pipettes filled with a K-gluconate internal solution. Atropine was present in all recordings to suppress muscarinic ACh receptor activity. QX-314 was typically included in the internal solution for improved voltage control. Photostimulation of ChR2 during recordings was executed using a 40× (0.8 NA) objective, a light-emitting diode (LED) light source, and TTL pulses delivered from the recording/acquisition software. Drugs were delivered to the slice via bath application (superfusion) or directly to the recorded cell via pressure ejection from an adjacent drug-filled pipette.

Two-Photon Imaging and Nicotine Uncaging

Brain slices were imaged via two-photon excitation microscopy using an Olympus BX51 microscope with a 60× (1.0 NA) objective. Infrared excitation light was provided via a Ti:sapphire laser system (Mai Tai HP1040; Spectra Physics), and non-de-scanned fluorescence emission was acquired via dual photomultiplier tubes. The microscope was equipped with a dual scanhead; one x-y galvanometer mirror system controlled the imaging laser beam while another x-y galvanometer system independently positioned a photostimulation (405 nm; OBIS FP LX; Coherent) beam for photolysis of PA-Nic (Banala et al., 2018). For two-photon experiments, all aspects of imaging, photostimulation, and recording were conducted using Prairie View 5.4 software (Bruker Nano).

Statistics and Data Analysis

The α level was set to 0.05 for all statistical tests, which were conducted with GraphPad Prism 7 software. Statistical tests included two-sided unpaired Student's t test, two-sided paired t test, and ANOVA. Error bars denote SEM or SD, as indicated in figure legends. Image analysis was performed with ImageJ. Analysis of electrophysiological data was performed with Clampfit (Molecular Devices) and custom scripts written in MATLAB (The MathWorks). Throughout the figure legends, the number of individual neurons tested is stated immediately before the number of animals from which those neurons were derived.

SUPPLEMENTAL INFORMATION

Supplemental Information includes Supplemental Experimental Procedures, four figures, and two tables and can be found with this article online at https://doi.org/10.1016/j.celrep.2018.04.062.

ACKNOWLEDGMENTS

This work was supported by NIH grants (DA035942, DA040626, DA045507, and DA030396 to R.M.D.; GM103801 and GM48677 to J.M.M.; and DA028955 to H.A. Lester), the Howard Hughes Medical Institute, and Northwestern University. M.C.A. was supported by a PhRMA Foundation fellowship. D.L.W. was supported by the JPB Foundation. We thank the following investigators at Northwestern University for technical assistance, discussion, and mouse strains: D.J. Surmeier, C.S. Chan, L. Parisiadou, Y. Kozorovitskiy, and A. Contractor. We thank the lab of H.A. Lester (California Institute of Technology) for providing mouse strains.

AUTHOR CONTRIBUTIONS

Conceptualization, R.M.D.; Methodology, Y.Y., C.P., M.C.A., X.-T.J., Y.W., D.L.W., and R.M.D.; Software, R.M.D.; Validation, Y.Y., C.P., M.C.A., X.-T.J., M.D.R., Y.W., and D.L.W.; Formal Analysis, R.M.D.; Investigation, Y.Y., C.P., M.C.A., X.-T.J., Y.W., and R.M.D.; Resources, S.B., V.J.K., L.D.L., and J.M.M.; Data Curation, R.M.D.; Writing – Original Draft, R.M.D.; Writing – Review & Editing, Y.Y., C.P., M.C.A., X.-T.J., Y.W., D.L.W., J.M.M., and R.M.D.; Visualization, R.M.D.; Supervision, R.M.D.; Project Administration, R.M.D.; Funding Acquisition, R.M.D.

DECLARATION OF INTERESTS

Conotoxins used in this study have been patented by the University of Utah with J.M.M. listed as an inventor.

Received: December 28, 2017
Revised: March 12, 2018
Accepted: April 15, 2018
Published: May 22, 2018

REFERENCES

Banala, S., Arvin, M.C., Bannon, N.M., Jin, X.T., Macklin, J.J., Wang, Y., Peng, C., Zhao, G., Marshall, J.J., Gee, K.R., et al. (2018). Photoactivatable drugs for nicotinic optopharmacology. Nat. Methods *15*, 347–350.

Brazell, M.P., Mitchell, S.N., Joseph, M.H., and Gray, J.A. (1990). Acute administration of nicotine increases the in vivo extracellular levels of dopamine, 3,4-dihydroxyphenylacetic acid and ascorbic acid preferentially in the nucleus accumbens of the rat: comparison with caudate-putamen. Neuropharmacology *29*, 1177–1185.

Calabresi, P., Lacey, M.G., and North, R.A. (1989). Nicotinic excitation of rat ventral tegmental neurones in vitro studied by intracellular recording. Br. J. Pharmacol. *98*, 135–140.

Champtiaux, N., Han, Z.Y., Bessis, A., Rossi, F.M., Zoli, M., Marubio, L., McIntosh, J.M., and Changeux, J.P. (2002). Distribution and pharmacology of α6-containing nicotinic acetylcholine receptors analyzed with mutant mice. J. Neurosci. *22*, 1208–1217.

Dautan, D., Souza, A.S., Huerta-Ocampo, I., Valencia, M., Assous, M., Witten, I.B., Deisseroth, K., Tepper, J.M., Bolam, J.P., Gerdjikov, T.V., and Mena-Segovia, J. (2016). Segregated cholinergic transmission modulates dopamine neurons integrated in distinct functional circuits. Nat. Neurosci. *19*, 1025–1033.

Dobi, A., Margolis, E.B., Wang, H.L., Harvey, B.K., and Morales, M. (2010). Glutamatergic and nonglutamatergic neurons of the ventral tegmental area establish local synaptic contacts with dopaminergic and nondopaminergic neurons. J. Neurosci. *30*, 218–229.

Drenan, R.M., Grady, S.R., Whiteaker, P., McClure-Begley, T., McKinney, S., Miwa, J.M., Bupp, S., Heintz, N., McIntosh, J.M., Bencherif, M., et al. (2008). In vivo activation of midbrain dopamine neurons via sensitized, high-affinity α6 nicotinic acetylcholine receptors. Neuron *60*, 123–136.

Engle, S.E., Broderick, H.J., and Drenan, R.M. (2012). Local application of drugs to study nicotinic acetylcholine receptor function in mouse brain slices. J. Vis. Exp. (*68*), e50034.

Faget, L., Osakada, F., Duan, J., Ressler, R., Johnson, A.B., Proudfoot, J.A., Yoo, J.H., Callaway, E.M., and Hnasko, T.S. (2016). Afferent inputs to neurotransmitter-defined cell types in the ventral tegmental area. Cell Rep. *15*, 2796–2808.

Hnasko, T.S., Hjelmstad, G.O., Fields, H.L., and Edwards, R.H. (2012). Ventral tegmental area glutamate neurons: electrophysiological properties and projections. J. Neurosci. *32*, 15076–15085.

Kenny, P.J., Chartoff, E., Roberto, M., Carlezon, W.A., Jr., and Markou, A. (2009). NMDA receptors regulate nicotine-enhanced brain reward function and intravenous nicotine self-administration: role of the ventral tegmental area and central nucleus of the amygdala. Neuropsychopharmacology *34*, 266–281.

Klink, R., de Kerchove d'Exaerde, A., Zoli, M., and Changeux, J.P. (2001). Molecular and physiological diversity of nicotinic acetylcholine receptors in the midbrain dopaminergic nuclei. J. Neurosci. *21*, 1452–1463.

Mackey, E.D., Engle, S.E., Kim, M.R., O'Neill, H.C., Wageman, C.R., Patzlaff, N.E., Wang, Y., Grady, S.R., McIntosh, J.M., Marks, M.J., et al. (2012). α6* nicotinic acetylcholine receptor expression and function in a visual salience circuit. J. Neurosci. *32*, 10226–10237.

Mansvelder, H.D., and McGehee, D.S. (2000). Long-term potentiation of excitatory inputs to brain reward areas by nicotine. Neuron *27*, 349–357.

Mansvelder, H.D., Keath, J.R., and McGehee, D.S. (2002). Synaptic mechanisms underlie nicotine-induced excitability of brain reward areas. Neuron *33*, 905–919.

Ntamati, N.R., and Lüscher, C. (2016). VTA projection neurons releasing GABA and glutamate in the dentate gyrus. eNeuro *3*, 3.

Pidoplichko, V.I., DeBiasi, M., Williams, J.T., and Dani, J.A. (1997). Nicotine activates and desensitizes midbrain dopamine neurons. Nature *390*, 401–404.

Qi, J., Zhang, S., Wang, H.L., Barker, D.J., Miranda-Barrientos, J., and Morales, M. (2016). VTA glutamatergic inputs to nucleus accumbens drive aversion by acting on GABAergic interneurons. Nat. Neurosci. *19*, 725–733.

Root, D.H., Mejias-Aponte, C.A., Qi, J., and Morales, M. (2014a). Role of glutamatergic projections from ventral tegmental area to lateral habenula in aversive conditioning. J. Neurosci. *34*, 13906–13910.

Root, D.H., Mejias-Aponte, C.A., Zhang, S., Wang, H.L., Hoffman, A.F., Lupica, C.R., and Morales, M. (2014b). Single rodent mesohabenular axons release glutamate and GABA. Nat. Neurosci. *17*, 1543–1551.

Shih, P.Y., Engle, S.E., Oh, G., Deshpande, P., Puskar, N.L., Lester, H.A., and Drenan, R.M. (2014). Differential expression and function of nicotinic acetylcholine receptors in subdivisions of medial habenula. J. Neurosci. *34*, 9789–9802.

Stamatakis, A.M., Jennings, J.H., Ung, R.L., Blair, G.A., Weinberg, R.J., Neve, R.L., Boyce, F., Mattis, J., Ramakrishnan, C., Deisseroth, K., and Stuber, G.D. (2013). A unique population of ventral tegmental area neurons inhibits the lateral habenula to promote reward. Neuron *80*, 1039–1053.

Stuber, G.D., Hnasko, T.S., Britt, J.P., Edwards, R.H., and Bonci, A. (2010). Dopaminergic terminals in the nucleus accumbens but not the dorsal striatum corelease glutamate. J. Neurosci. *30*, 8229–8233.

Wallace, M.L., Saunders, A., Huang, K.W., Philson, A.C., Goldman, M., Macosko, E.Z., McCarroll, S.A., and Sabatini, B.L. (2017). Genetically distinct parallel pathways in the entopeduncular nucleus for limbic and sensorimotor output of the basal ganglia. Neuron *94*, 138–152.e5.

Wang, H.L., Qi, J., Zhang, S., Wang, H., and Morales, M. (2015). Rewarding effects of optical stimulation of ventral tegmental area glutamatergic neurons. J. Neurosci. *35*, 15948–15954.

Xiao, C., Cho, J.R., Zhou, C., Treweek, J.B., Chan, K., McKinney, S.L., Yang, B., and Gradinaru, V. (2016). Cholinergic mesopontine signals govern locomotion and reward through dissociable midbrain pathways. Neuron *90*, 333–347.

Yamaguchi, T., Sheen, W., and Morales, M. (2007). Glutamatergic neurons are present in the rat ventral tegmental area. Eur. J. Neurosci. *25*, 106–118.

Yoo, J.H., Zell, V., Gutierrez-Reed, N., Wu, J., Ressler, R., Shenasa, M.A., Johnson, A.B., Fife, K.H., Faget, L., and Hnasko, T.S. (2016). Ventral tegmental area glutamate neurons co-release GABA and promote positive reinforcement. Nat. Commun. *7*, 13697.

Zhang, S., Qi, J., Li, X., Wang, H.L., Britt, J.P., Hoffman, A.F., Bonci, A., Lupica, C.R., and Morales, M. (2015). Dopaminergic and glutamatergic microdomains in a subset of rodent mesoaccumbens axons. Nat. Neurosci. *18*, 386–392.

Cell Reports, Volume *23*

Supplemental Information

Nicotinic Cholinergic Receptors in VTA Glutamate Neurons Modulate Excitatory Transmission

Yijin Yan, Can Peng, Matthew C. Arvin, Xiao-Tao Jin, Veronica J. Kim, Matthew D. Ramsey, Yong Wang, Sambashiva Banala, David L. Wokosin, J. Michael McIntosh, Luke D. Lavis, and Ryan M. Drenan

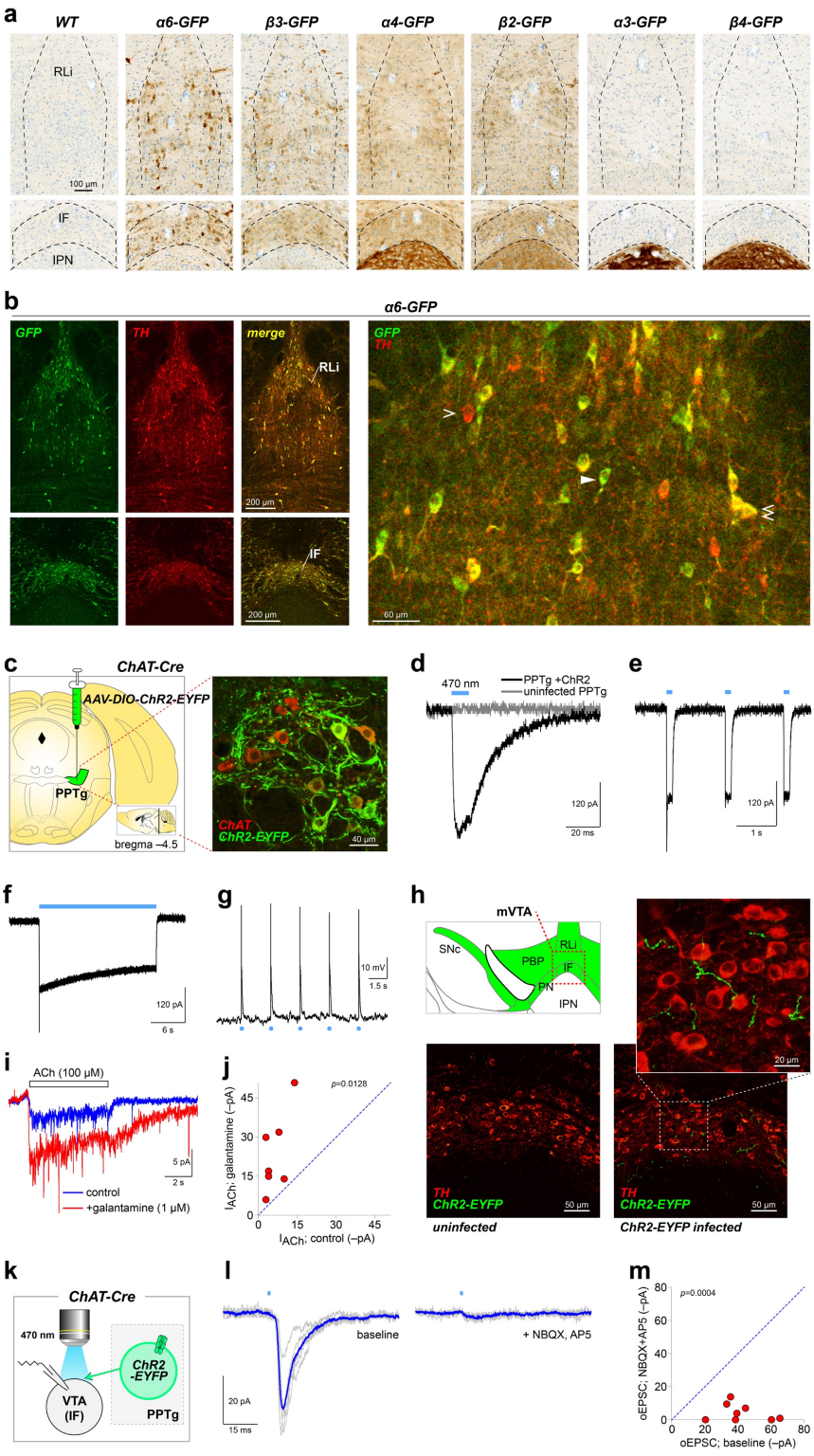

Figure S1. Related to Figure 1 – Supplemental data and opsin validation controls. (**a**) mVTA nuclei express nAChRs. Coronal sections containing mVTA structures (RLi: rostral linear nucleus; IF: interfascicular nucleus) dorsal to the interpeduncular nucleus (IPN) from knock-in/transgenic mice expressing the indicated GFP-fused nAChR subunit were stained with anti-GFP antibodies and visualized with DAB staining. Representative of n=3 mice. (**b**) The RLi and IF in coronal sections from α6-GFP mice were co-stained with anti-GFP and anti-tyrosine

hydroxylase (TH) antibodies (left panels). A high-magnification image through the RLi is shown (right panel), with TH+/α6− (single open arrowhead), TH−/α6+ (single closed arrowhead), and TH+/α6+ neurons (double open arrowhead). (**c**) AAVs directing Cre-dependent expression of ChR2-EYFP were bilaterally injected into PPTg of ChAT-Cre mice at the approximate location indicated (left panel). Coronal sections from infected animals were stained with anti-ChAT and anti-GFP antibodies (right panel) to verify ChR2 expression in ChAT neurons. (**d-f**) Photocurrents were recorded in voltage-clamped PPTg neurons expressing ChR2. Brief (10 ms), intermediate (100 ms), and prolonged (20 s) light (470 nm, 0.12 mW/mm^2) pulses demonstrate ChR2 functionality. (**g**) ChR2 activation drives action potential firing. A ChR2-expressing PPTg ChAT neuron was held in current clamp (I=0) configuration and repetitively stimulated with brief (0.1 ms) light flashes (0.12 mW/mm^2) to elicit action potentials. (**h**) Expression of ChR2 in mVTA fibers. Coronal sections containing mVTA (top left; SNc: substantia nigra pars compacta, PBP: parabrachial pigmented nucleus, PN: paranigral nucleus, IF: interfascicular nucleus, RLi: rostral linear nucleus) from ChAT-Cre mice infected as described in (c) were stained with anti-TH and anti-GFP antibodies to visualize ChR2 expression in cholinergic fibers (top/bottom right). Specificity of detection is provided via uninfected control sections (bottom left). (**i,j**) Galantamine validation. Voltage-clamped mVTA glutamate neurons (n=7 cells/3 mice) were stimulated with pressure ejection application of ACh (100 μM, 5 s, 1-2 psi) to mimic ChR2-mediated ACh release kinetics (**Fig. 1f**). Addition of galantamine potentiated ACh-evoked currents (i). (j) Plot for individual VTA glutamate neurons showing ACh-evoked current amplitude before (control) and after galantamine bath application. *P* value: two-sided paired *t*-test. (**k**) AAV-ChR2-EYFP vectors were microinjected into PPTg to express ChR2 non-specifically in this nucleus. Optical EPSCs (oEPSCs) were recorded in IF VTA neurons; results in (l,m). (**l**) oEPSCs in an IF VTA neuron before and after addition of NBQX (10 μM) + D-AP5 (20 μM). Individual sweeps (grey traces) and an average trace (blue trace) are shown. Representative of (n=8 cells/3 mice). (**m**) Plot for individual IF VTA neurons showing oEPSC amplitude before (baseline) and after bath application of NBQX (10 μM) + D-AP5 (20 μM). *P* value: two-sided paired *t*-test.

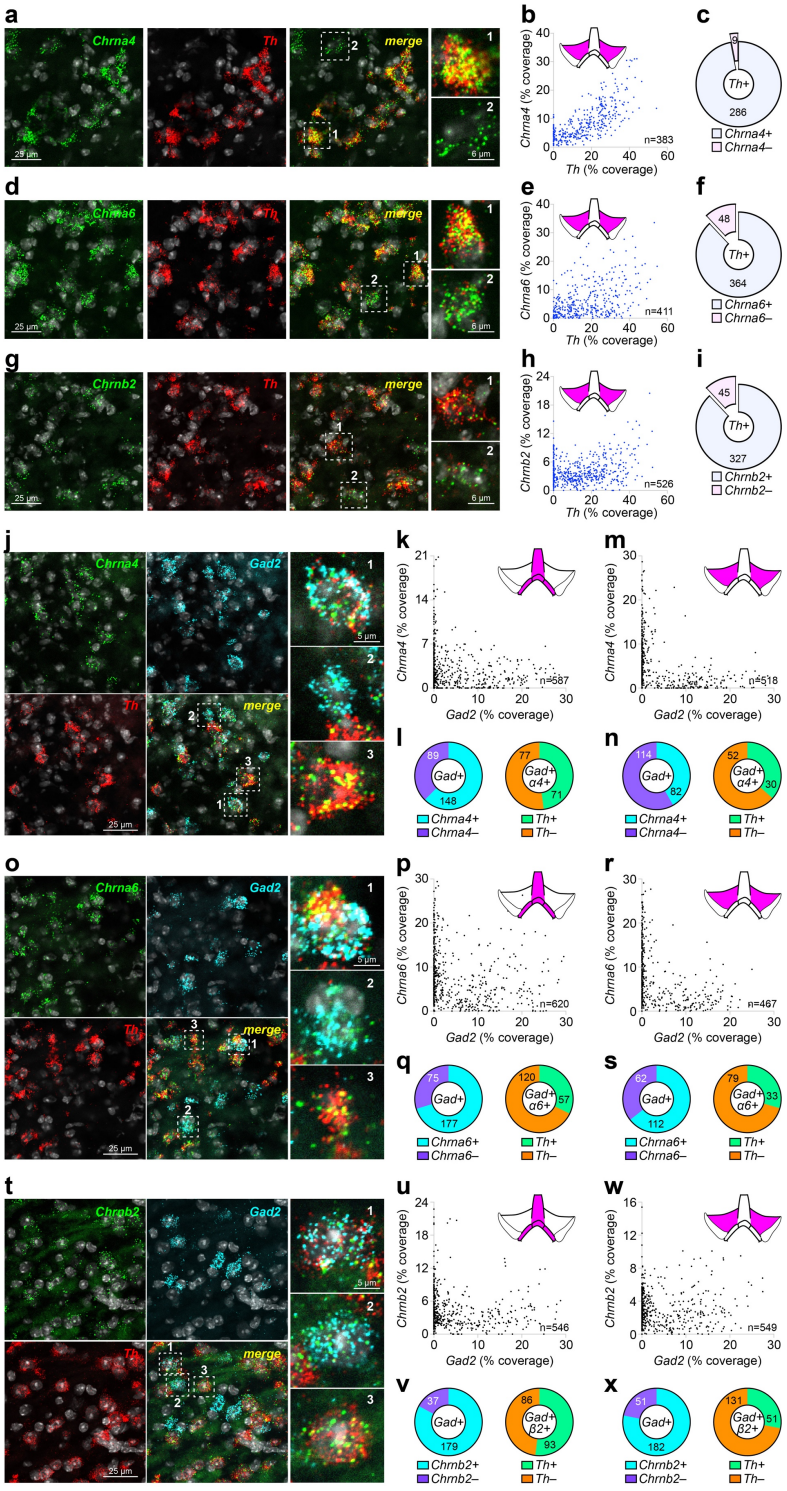

Figure S2. Related to Figure 2 – Supplemental FISH controls and data. (**a-c**) *Chrna4* FISH probe validation. (a) Representative 2-channel fluorescence *in situ* hybridization (FISH) images in lateral VTA neurons for probes: *Chrna4*, *Th*. Single *Chrna4*+ neurons indicated in the 'merge' panel, and shown enlarged (right panels), had this expression profile: 1) *Chrna4*+/*Th*+; 2) *Chrna4*+/*Th*−. (b-c) Analysis of *Chrna4*/*Th* co-expression in lateral VTA. (b) Scatter plots showing *Th* (abscissa) and *Chrna4* (ordinate) '% coverage' for all analyzed neurons. (c) Pie graph showing the fraction of *Th*+ neurons that were *Chrna4*+ vs. *Chrna4*−. (**d-f**) *Chrna6* FISH probe validation. Analysis

for *Chrna6* were performed as for *Chrna4*. (**g-i**) *Chrnb2* FISH probe validation. Analysis for *Chrnb2* were performed as for *Chrna4* and *Chrna6*. Data are pooled from n=3 mice. (**j-n**) Co-expression of *Chrna4* and *Gad2* in VTA neurons. (**j**) Representative 3-channel fluorescence *in situ* hybridization (FISH) images in mVTA neurons for the following probes: *Chrna4*, *Gad2*, and *Th*. Single *Chrna4*+ neurons indicated in the 'merge' panel, and shown enlarged (right panels), had this expression profile: 1) *Chrna4*+/*Gad2*+/*Th*+; 2) *Chrna4*+/*Gad2*+/*Th*−; 3) *Chrna4*+/*Gad2*−/*Th*+. (**k-l**) Analysis of *Chrna4*/*Gad2* co-expression in mVTA. (**k**) Scatter plots showing *Gad2* (abscissa) and *Chrna4* (ordinate) '% coverage' for all analyzed neurons. (**l**) Left: Pie graph showing the fraction of *Gad2*+ neurons that were *Chrna4*+ vs. *Chrna4*−. Right: *Th* expression status is shown for *Gad2*+/*Chrna4*+ neurons from left graph. (**m-n**) Analysis of *Chrna4*/*Gad2* co-expression in lateral VTA was performed as in mVTA (k-l). (**o-s**) Co-expression of *Chrna6* and *Gad2* in VTA neurons. Analysis for *Chrna6* were performed as for *Chrna4*. (**t-x**) Co-expression of *Chrnb2* and *Gad2* in VTA neurons. Analysis for *Chrnb2* were performed as for *Chrna4* and *Chrna6*. Complete data for nAChR/*Gad2* FISH is listed in **Table S2**. Data are pooled from n=3 mice.

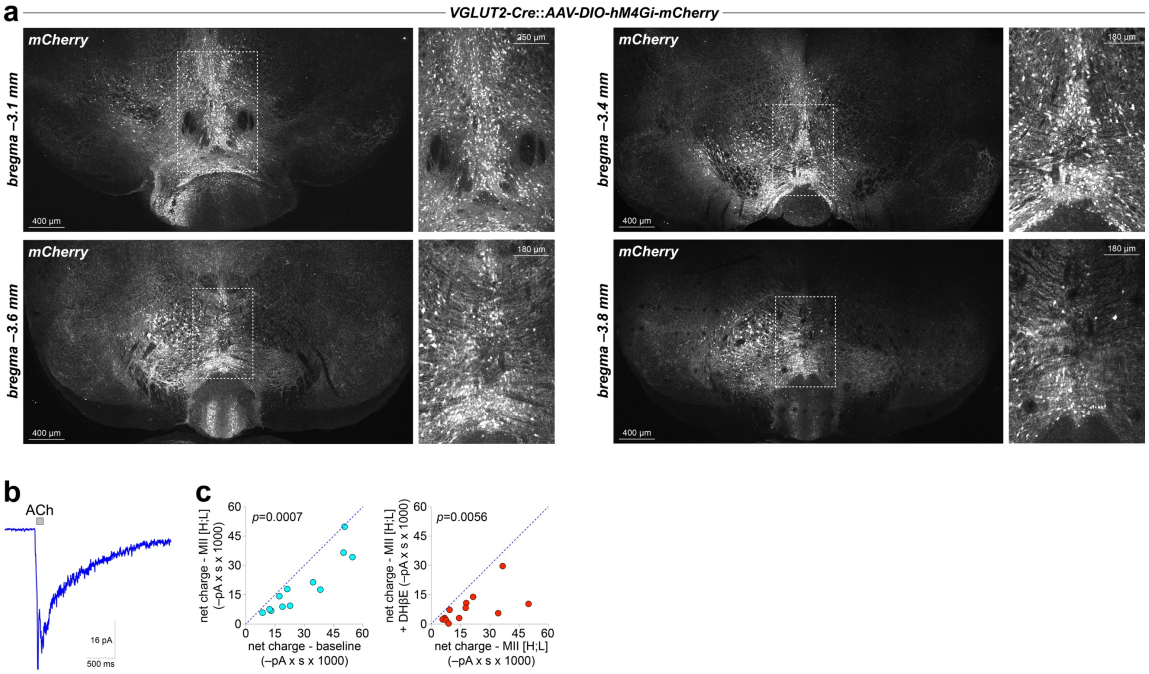

Figure S3. Related to Figure 3 – Controls for functional nAChR measurements in VGLUT2+ neurons. (**a**) Widefield images of ventral midbrain in VGLUT2-Cre mice microinjected in mVTA with AAV-DIO-hM4Gi-mCherry viral constructs. Anti-DsRed immunostaining was performed on coronal sections at the indicated bregma level. Boxed areas are shown enlarged immediately at right. Representative of n>70 mice. Micrograph for bregma −3.4 mm is also shown in **Fig. 3** in color and at higher zoom; it was shown here to allow a complete disclosure of hM4Gi-mCherry expression across the rostral-caudal extent of the VTA. (**b**) Averaged trace for pressure ejection applications of 1 mM ACh to mVTA neurons in slices from unlabeled/non-Cre C57BL/6 mice. (**c**) Left: 1 mM ACh-induced net charge at baseline vs. after bath application of α-Ctx MII[H9A;L15A] for (n=9 cells/5 mice) mVTA neurons from unlabeled/non-Cre C57BL/6 mice. Right: 1 mM ACh-induced net charge in the presence of α-Ctx MII[H9A;L15A] vs. α-Ctx MII[H9A;L15A] + 1 µM DHβE for the same neurons shown at left. *P* values: two-sided paired *t*-test.

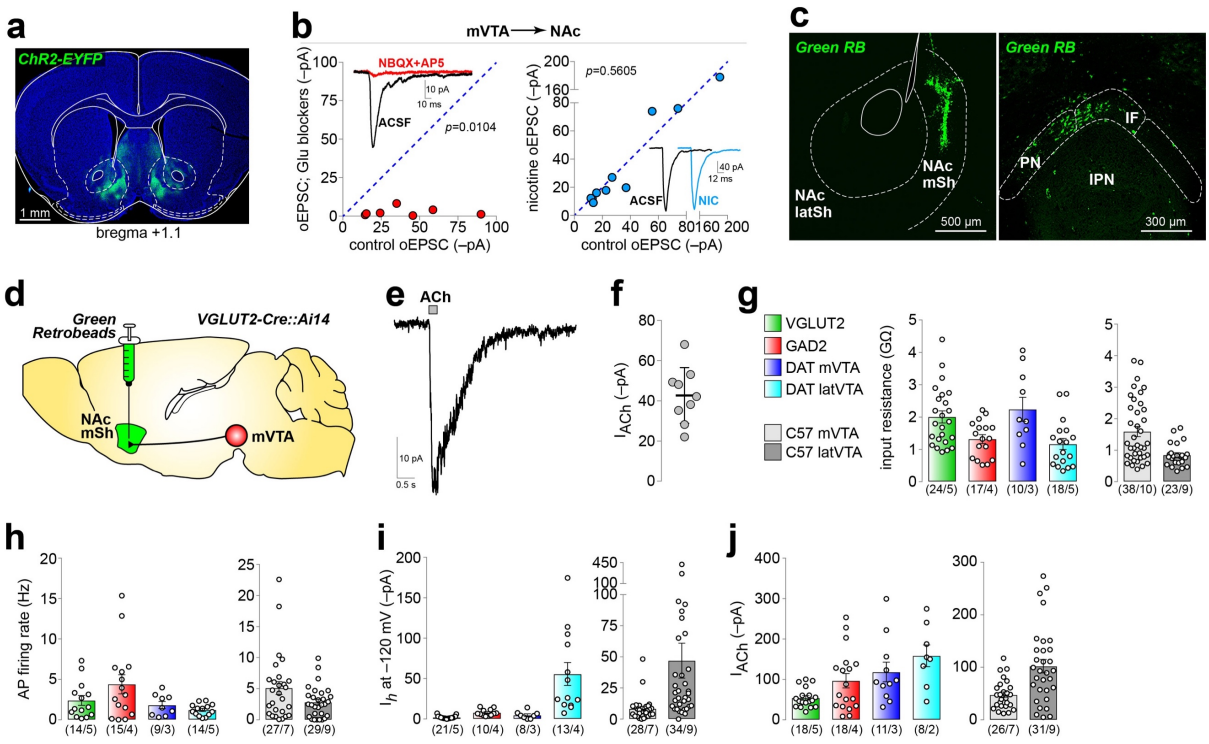

Figure S4. Related to Figure 4 - NAc glutamate transmission and electrophysiological properties of midbrain neurons. (**a**) ChR2-EYFP expression in NAc medial shell after ChR2 virus microinjection into mVTA of VGLUT2-Cre mice. (**b**) Sensitivity of NAc oEPSCs to NBQX + D-AP5 (left; n=7 cells/3 mice). Summary data for NAc oEPSCs before/after nicotine (0.3 µM) bath application (right; n=10/5). *P* values: two-sided paired *t*-test. (**c**) Green retrobead injection site in NAc medial shell (left) and resulting labeled mVTA neurons (right). (**d**) Green retrobeads were injected into NAc medial shell of VGLUT2-Cre::Ai14 mice. (**e-f**) ACh (1 mM)-evoked currents were measured in mVTA neurons with dual green+red fluorescence (representative trace (e) and scatter plot (f) of all response amplitudes (mean ± s.d.; n=9/2). (**g-j**) Electrophysiological properties of mVTA neurons. Input resistance (g), action potential firing rate (h), I_h current at a holding potential of −120 mV (i), and peak current evoked by pressure ejection application of ACh (1 mM) (j) was measured in mVTA VGLUT2+, GAD2+, and DAT+ neurons in mVTA. DAT+ neurons in lateral VTA were also studied for comparison. The same properties were also measured in medial and lateral VTA neurons in slices from C57BL/6 WT mice. Number of cells and mice are indicated.

Table S1. Related to Figure 2 – Expression of *Chrna4*, *Chrna6*, and *Chrnb2* in VTA glutamate neurons. Full quantification of triple channel mRNA FISH experiments is shown for medial (top section) and lateral VTA (bottom section). All sections were probed for *Slc17a6* and *Th*, while either *Chrna4*, *Chrna6* or *Chrnb2* was probed in the 3rd channel.

Medial VTA												
	Total	Slc17a6(+)	Slc17a6(−)	Slc17a6(+)					Slc17a6(−)			
				TH(+)	TH(−)	TH(+)	TH(−)		TH(+)	TH(−)	TH(+)	TH(−)
				Chrna4(+)	Chrna4(+)	Chrna4(−)	Chrna4(−)		Chrna4(+)	Chrna4(+)	Chrna4(−)	Chrna4(−)
# cells->	443	257/443	186/443	138/257	71/257	11/257	37/257		153/186	21/186	7/186	5/186
fraction->		0.58	0.42	0.54	0.28	0.04	0.14		0.82	0.11	0.04	0.03
				TH(+)	TH(−)	TH(+)	TH(−)		TH(+)	TH(−)	TH(+)	TH(−)
				Chrna6(+)	Chrna6(+)	Chrna6(−)	Chrna6(−)		Chrna6(+)	Chrna6(+)	Chrna6(−)	Chrna6(−)
# cells->	524	305/524	219/524	188/305	50/305	17/305	50/305		150/219	21/219	34/219	14/219
fraction->		0.58	0.42	0.62	0.16	0.06	0.16		0.68	0.10	0.16	0.06
				TH(+)	TH(−)	TH(+)	TH(−)		TH(+)	TH(−)	TH(+)	TH(−)
				Chrnb2(+)	Chrnb2(+)	Chrnb2(−)	Chrnb2(−)		Chrnb2(+)	Chrnb2(+)	Chrnb2(−)	Chrnb2(−)
# cells->	510	372/510	138/510	181/372	109/372	33/372	49/372		71/138	27/138	27/138	13/138
fraction->		0.73	0.27	0.49	0.29	0.09	0.13		0.51	0.20	0.20	0.09

Lateral VTA												
	Total	Slc17a6(+)	Slc17a6(−)	Slc17a6(+)					Slc17a6(−)			
				TH(+)	TH(−)	TH(+)	TH(−)		TH(+)	TH(−)	TH(+)	TH(−)
				Chrna4(+)	Chrna4(+)	Chrna4(−)	Chrna4(−)		Chrna4(+)	Chrna4(+)	Chrna4(−)	Chrna4(−)
# cells->	596	191/596	405/596	99/191	32/191	5/191	55/191		353/405	35/405	8/405	9/405
fraction->		0.32	0.68	0.52	0.17	0.03	0.29		0.87	0.09	0.02	0.02
				TH(+)	TH(−)	TH(+)	TH(−)		TH(+)	TH(−)	TH(+)	TH(−)
				Chrna6(+)	Chrna6(+)	Chrna6(−)	Chrna6(−)		Chrna6(+)	Chrna6(+)	Chrna6(−)	Chrna6(−)
# cells->	534	177/534	357/534	50/177	50/177	3/177	74/177		256/357	65/357	19/357	17/357
fraction->		0.33	0.67	0.28	0.28	0.02	0.42		0.72	0.18	0.05	0.05
				TH(+)	TH(−)	TH(+)	TH(−)		TH(+)	TH(−)	TH(+)	TH(−)
				Chrnb2(+)	Chrnb2(+)	Chrnb2(−)	Chrnb2(−)		Chrnb2(+)	Chrnb2(+)	Chrnb2(−)	Chrnb2(−)
# cells->	539	200/539	339/539	50/200	100/200	13/200	37/200		177/339	73/339	78/339	11/339
fraction->		0.37	0.63	0.25	0.50	0.07	0.19		0.52	0.22	0.23	0.03

Table S2. Related to Figure 2 – Expression of *Chrna4*, *Chrna6*, and *Chrnb2* in VTA GABA neurons. Full quantification of triple channel mRNA FISH experiments is shown for medial (top section) and lateral VTA (bottom section). All sections were probed for *Gad2* and *Th*, while either *Chrna4*, *Chrna6* or *Chrnb2* was probed in the 3rd channel.

Medial VTA												
	Total	Gad2(+)	Gad2(−)	Gad2(+)					Gad2(−)			
				TH(+)	TH(−)	TH(+)	TH(−)		TH(+)	TH(−)	TH(+)	TH(−)
				Chrna4(+)	Chrna4(+)	Chrna4(−)	Chrna4(−)		Chrna4(+)	Chrna4(+)	Chrna4(−)	Chrna4(−)
# cells->	587	237/587	350/587	71/237	77/237	15/237	74/237		253/350	21/350	71/350	5/350
fraction->		0.40	0.60	0.30	0.32	0.06	0.31		0.72	0.06	0.20	0.01
				TH(+)	TH(−)	TH(+)	TH(−)		TH(+)	TH(−)	TH(+)	TH(−)
				Chrna6(+)	Chrna6(+)	Chrna6(−)	Chrna6(−)		Chrna6(+)	Chrna6(+)	Chrna6(−)	Chrna6(−)
# cells->	620	252/620	368/620	57/252	120/252	6/252	69/252		298/368	51/368	14/368	5/368
fraction->		0.41	0.59	0.23	0.48	0.02	0.27		0.81	0.14	0.04	0.01
				TH(+)	TH(−)	TH(+)	TH(−)		TH(+)	TH(−)	TH(+)	TH(−)
				Chrnb2(+)	Chrnb2(+)	Chrnb2(−)	Chrnb2(−)		Chrnb2(+)	Chrnb2(+)	Chrnb2(−)	Chrnb2(−)
# cells->	546	216/546	330/546	93/216	86/216	6/216	31/216		272/330	39/330	18/330	1/330
fraction->		0.40	0.60	0.43	0.40	0.03	0.14		0.82	0.12	0.05	0.00

Lateral VTA												
	Total	Gad2(+)	Gad2(−)	Gad2(+)					Gad2(−)			
				TH(+)	TH(−)	TH(+)	TH(−)		TH(+)	TH(−)	TH(+)	TH(−)
				Chrna4(+)	Chrna4(+)	Chrna4(−)	Chrna4(−)		Chrna4(+)	Chrna4(+)	Chrna4(−)	Chrna4(−)
# cells->	518	196/518	322/518	30/196	52/196	9/196	105/196		276/322	9/322	34/322	3/322
fraction->		0.38	0.62	0.15	0.27	0.05	0.54		0.86	0.03	0.11	0.01
				TH(+)	TH(−)	TH(+)	TH(−)		TH(+)	TH(−)	TH(+)	TH(−)
				Chrna6(+)	Chrna6(+)	Chrna6(−)	Chrna6(−)		Chrna6(+)	Chrna6(+)	Chrna6(−)	Chrna6(−)
# cells->	467	174/467	293/467	33/174	79/174	6/174	56/174		254/293	22/293	15/293	2/293
fraction->		0.37	0.63	0.19	0.45	0.03	0.32		0.87	0.08	0.05	0.01
				TH(+)	TH(−)	TH(+)	TH(−)		TH(+)	TH(−)	TH(+)	TH(−)
				Chrnb2(+)	Chrnb2(+)	Chrnb2(−)	Chrnb2(−)		Chrnb2(+)	Chrnb2(+)	Chrnb2(−)	Chrnb2(−)
# cells->	549	233/549	316/549	51/233	131/233	2/233	49/233		256/316	35/316	23/316	2/316
fraction->		0.42	0.58	0.22	0.56	0.01	0.21		0.81	0.11	0.07	0.01

Supplemental Experimental Procedures

Materials and Viral Vectors - AAV9.EF1a.ChR2-EYFP.WPRE.hGH, AAV9.EF1a.DIO.hChR2(H134R)-eYFP.WPRE.hGH and AAV9.EF1a.DIO.hChR2(H134R)-mCherry.WPRE.hGH were obtained from Penn Vector Core. AAV5.hSyn.DIO.hM4D(Gi)-mCherry.WPRE.hGH was from Addgene. AAV5/2.U6-control-sgRNA.hSyn.mCherry.WPRE.SV40pA (sgRNA target sequence: 5′-GCGAGGTATTCGGCTCCGCG-3′) and AAV5/2.U6-Chrnb2-sgRNA.hSyn.mCherry.WPRE.SV40pA (sgRNA target sequence: 5′-ATCAGCTTGTTATAGCGGGA-3′) custom viruses were produced by Virovek, Inc. α-conotoxins were synthesized as previously described (Azam et al., 2010). Dihydro-β-erythroidine hydrobromide (DHβE), methyllycaconitine (MLA), picrotoxin, and atropine sulfate (atropine) were obtained from Sigma. 6-Cyano-7-nitroquinoxaline-2,3-dione (CNQX), 2,3-Dioxo-6-nitro-1,2,3,4-tetrahydrobenzo[*f*]quinoxaline-7-sulfonamide (NBQX), D-(-)-2-Amino-5-phosphonopentanoic acid (D-AP5), Octahydro-12-(hydroxymethyl)-2-imino-5,9:7,10a-dimethano-10aH-[1,3]dioxocino[6,5-d]pyrimidine-4,7,10,11,12-pentol (TTX), QX314 chloride (QX314), and galantamine hydrobromide (galantamine) were obtained from Tocris. Alexafluor (Alexa) 488 was obtained from Life Technologies. Green retrobeads IX were obtained from Lumafluor, Inc. PA-Nic was synthesized as previously described (Banala et al., 2018).

Stereotaxic Surgery - Male and female mice were used for surgery starting at 8 weeks of age. Mice were initially anesthetized with an intraperitoneal (i.p.) injection of a ketamine/xylazine mixture (120 mg/kg ketamine, 16 mg/kg xylazine). Mice were given additional "boost" injections of ketamine (100 mg/kg, i.p.) as needed. Alternatively, some mice were anesthetized with isoflurane: 3% (flow rate 500 mL/min) for induction and 1.5% (28 mL/min) for maintenance. Mice were secured into a stereotaxic frame and a small incision at the top of the head was made to expose the skull. Coordinates (unilateral) used for mVTA injections were (relative to bregma, in mm): M/L: +0.01 (or −0.01), A/P: −3.2, D/V: −4.55. Coordinates (bilateral) used for lateral VTA injections were (relative to bregma, in mm): M/L: ±0.5, A/P: −3.2, D/V: −4.75. Coordinates (bilateral) used for PPTg were (relative to bregma, in mm): M/L: ±1.20, A/P: −4.45, D/V: −4.05. Coordinates (unilateral) used for nucleus accumbens medial shell were (relative to bregma, in mm): M/L: ±0.5, A/P: +1.3, D/V: −4.75. Exact coordinates were adjusted to account for slight differences in the head size of individual mice: the bregma/lambda distance measured for each mouse was divided by the reported bregma/lambda distance for C57 mice (4.21), then multiplied by the A/P coordinate. The injection needle was slowly lowered through the drilled hole to the D/V coordinate. For AAV viruses, 500 nL of virus was infused at a rate of 50 nL/min. For bilateral retrobead infusions, 500 nL/hemisphere was infused at a rate of 50 nL/min. For all stereotaxic injections, the injection needle was left in place for 10 min after the infusion ended before slowly retracting the needle. Sutures were used to close the incision. At the conclusion of the surgery, mice were given ketoprofen (5 mg/kg, s.c.) and placed in a recovery cage, kept warm, and observed until they were ambulatory. Mice were single-housed following virus injection surgery and were given at least 14 days to recover and for the virus to express before beginning experimental procedures. For electrophysiology experiments, accurate targeting of VTA was determined via direct visualization of fluorescent neurons in brain slices during recordings.

Immunohistochemistry and Confocal Microscopy - Anti-GFP immunostaining and visualization with 3,3'-diaminobenzidine (DAB) of nAChR-GFP knockin/transgenic mouse brains (**Fig. S1a**) was performed as part of the same tissue analysis as we previously described (Shih et al., 2014). All other immunohistochemistry in the paper was performed as follows. Mice were anesthetized with sodium pentobarbital (200 mg/kg, i.p.) and transcardially perfused with 10 mL of heparin-containing phosphate buffered saline (PBS) followed by 30 mL of 4% paraformaldehyde. Brains were dissected and postfixed in 4% paraformaldehyde overnight at 4°C. Coronal brain slices (50 μm) were cut on a freezing sliding microtome (SM2010R; Leica). VTA-containing slices were stained using the following procedure. Slices were first permeabilized for 2 min via incubation in PBST (0.3% Triton X-100 in PBS), followed by a 60 min incubation in blocking solution (0.1% Triton X-100, 5% horse serum in Tris-buffered saline (TBS)). Primary antibodies used in this study were as follows: sheep anti-TH (Millipore AB1542), rabbit anti-GFP (Invitrogen A11122), rabbit anti-DsRed (Clontech 632496), goat anti-ChAT (Millipore AB144P). Primary antibodies were diluted in blocking solution (anti-TH at 1:800, anti-GFP at 1:500, anti-DsRed at 1:500, anti-ChAT at 1:100). Slices were incubated in primary antibodies overnight at 4°C. Three 5 min washes in TBST (0.1% Triton X-100 in TBS) were done before transferring slices to secondary antibodies for a 60 min incubation at room temperature (anti-sheep or anti-rabbit Alexa 555, anti-rabbit Alexa 488, diluted to 1:500 in blocking solution). Slices were washed as before, mounted on slides, and coverslipped with Vectashield. Staining in the VTA was imaged as previously described (Mackey et al., 2012) with a Nikon A1 laser-scanning confocal microscope.

mRNA fluorescence in situ hybridization and image analysis - Mice were deeply anesthetized with sodium pentobarbital (200 mg/kg, i.p.) and decapitated. Brains were quickly removed on ice, snap frozen, and embedded in cryo-embedding medium (OCT). Brains were sectioned on a cryostat (CM3050; Leica) into 20 µm sections, sections were adhered to Superfrost® Plus slides, and kept at −20℃ to dry for 60 min and stored at −80℃ until use. Sections were fixed with 4% paraformaldehyde and processed for RNAscope (Advanced Cell Diagnostics) multichannel fluorescent *in situ* hybridization (FISH) according to the manufacturer manual for Multiplex assays. Sections were counterstained with DAPI for 30 s at room temperature. Probes for detection of specific targets (*Chrna4*, *Chrna6*, *Chrnb2*, *Th*, *Slc17a6*, *Gad2*) were purchased from Advanced Cell Diagnostics (ACD; http://acdbio.com/). Probes for *Slc17a6*, *Gad2*, and *Th* were previously reported (Wallace et al., 2017; Xiao et al., 2017). Probes for *Chrna4*, *Chrna6,* and *Chrnb2* were validated by comparing co-expression of TH/nAChR subunit mRNA with previously reported analyses using labeled riboprobes (Azam et al., 2002). This prior study indicated that 80-90% of *Th*(+) neurons also expressed *Chrna4*, *Chrna6*, and *Chrnb2*. Consistent with this, we found that 97%, 88%, and 88% of *Th*(+) neurons in lateral VTA were also positive for *Chrna4*, *Chrna6*, and *Chrnb2*, respectively (**Fig. S2**).

Sections were imaged on a Nikon A1 confocal microscope according to the following parameters: 1024 x 1024 pixels, ~200 nm/pixel, 20x 0.75 NA objective. Nikon system images containing 3 or 4 channels were processed with custom scripts in ImageJ (NIH). All images to be used for FISH quantification were acquired and processed in the same manner. FISH quantification employed the "fluorescence coverage (%)" method (Wallace et al., 2017), which reports the fraction of fluorescent pixels to total pixels in a cellular region of interest (ROI). Multichannel images were opened and all channels (including Dapi staining to identify cellular locations) were overlaid. Background subtraction was performed on each channel separately, as follows. Each channel in multichannel images were opened and background was measured in ImageJ in an area of the image devoid of cells as indicated by Dapi staining. Background values for each channel were subtracted to form a new background-subtracted channel image. Using the background-subtracted image, ROIs were drawn manually around cells containing at least one fluorescent signal, and Dapi staining assisted in distinguishing individual cells from cell clusters. A binary image was then produced for each channel for quantitative analysis using the default algorithm in ImageJ (version 1.51n). The percentage of fluorescent pixels to total pixels within each ROI was determined. These data were used to create x vs. y plots of percent coverage for each probe/channel and each cell. To assign a cell as either positive or negative for expression of each probe, a percent coverage "cutoff" was used such that the percent coverage in a ROI had to meet or exceed the cutoff to be counted as positive for the probe. Cutoffs were determined *de novo* for each assay and imaging session to account for any differences in probe performance or tissue autofluorescence over time or across days. A minimum of 3 mice were sampled for each condition, and 3-6 images were analyzed per mouse and per VTA sub-region (medial vs. lateral VTA).

Brain Slice Preparation and Recording Solutions - Brain slices were prepared as previously described (Engle et al., 2012). Mice were anesthetized with Euthasol (sodium pentobarbital, 100 mg/kg; sodium phenytoin, 12.82 mg/kg) before trans-cardiac perfusion with oxygenated (95% O_2/5% CO_2), 4°C N-methyl-D-glucamine (NMDG)-based recovery solution that contains (in mM): 93 NMDG, 2.5 KCl, 1.2 NaH_2PO_4, 30 $NaHCO_3$, 20 HEPES, 25 glucose, 5 sodium ascorbate, 2 thiourea, 3 sodium pyruvate, 10 $MgSO_4 \cdot 7H_2O$, and 0.5 $CaCl_2 \cdot 2H_2O$; 300-310 mOsm; pH 7.3-7.4). Brains were immediately dissected after the perfusion and held in oxygenated, 4°C recovery solution for one minute before cutting a brain block containing the VTA and sectioning the brain with a vibratome (VT1200S; Leica). Coronal slices (200-250 µm) were sectioned through the VTA and transferred to oxygenated, 33°C recovery solution for 12 min. Slices were then kept in holding solution (containing in mM: 92 NaCl, 2.5 KCl, 1.2 NaH_2PO_4, 30 $NaHCO_3$, 20 HEPES, 25 glucose, 5 sodium ascorbate, 2 thiourea, 3 sodium pyruvate, 2 $MgSO_4 \cdot 7H_2O$, and 2 $CaCl_2 \cdot 2H_2O$; 300-310 mOsm; pH 7.3-7.4) for 60 min or more before recordings.

Brain slices were transferred to a recording chamber being continuously superfused at a rate of 1.5-2.0 mL/min with oxygenated 32°C recording solution. The recording solution contained (in mM): 124 NaCl, 2.5 KCl, 1.2 NaH_2PO_4, 24 $NaHCO_3$, 12.5 glucose, 2 $MgSO_4 \cdot 7H_2O$, and 2 $CaCl_2 \cdot 2H_2O$; 300-310 mOsm; pH 7.3-7.4). For all recordings, the recording solution was supplemented with 1 µM atropine to eliminate contributions from muscarinic ACh receptors. Patch pipettes were pulled from borosilicate glass capillary tubes (1B150F-4; World Precision Instruments) using a programmable microelectrode puller (P-97; Sutter Instrument). Tip resistance ranged from 5.0 to 10.0 MΩ when filled with internal solution. The following internal solution was used (in mM): 135 potassium gluconate, 5 EGTA, 0.5 $CaCl_2$, 2 $MgCl_2$, 10 HEPES, 2 MgATP, and 0.1 GTP; pH adjusted to 7.25 with Tris base; osmolarity adjusted to 290 mOsm with sucrose. For uncaging, this internal solution also contained QX-314 (2 mM) for improved voltage control.

Standard Patch Clamp Electrophysiology - Neurons within brain slices were first visualized with infrared or visible differential interference contrast (DIC), followed in some cases by fluorescence microscopy to identify neurons expressing fluorescent proteins or within range of fluorescent axons. Electrophysiology experiments were conducted using a Nikon Eclipse FN-1 or Scientifica SliceScope. A computer running pCLAMP 10 software was used to acquire whole-cell recordings along with a Multiclamp 700B or Axopatch 200B amplifier and an A/D converter (Digidata 1440A or Digidata 1550A). pClamp software, Multiclamp/Axopatch amplifiers, and Digitata A/D converters were from Molecular Devices. Data were sampled at 10 kHz and low-pass filtered at 1 kHz. Immediately prior to gigaseal formation, the junction potential between the patch pipette and the superfusion medium was nulled. Series resistance was uncompensated. A light emitting diode (LED) light source (XCite 110LED; Excelitas) coupled to excitation filters (400/40 nm, 470/40 nm, and 560/40 nm bandpass) was used to search for fluorescent neurons and, for optogenetic experiments involving ChR2, to stimulate the preparation with light flashes. Light flashes were triggered by pCLAMP via TTL pulses. Flash energy output from the LED was determined by calibration using a photodiode power sensor (Model S120C; Thor Labs). Optical pulse duration (0.5-5 ms) and flash strength (<0.01 mW/mm^2) were empirically chosen for each cell such that baseline responses were initially ~50-150 pA. Optical pulse duration and flash strength were longer/stronger (20 s, 0.12 mW/mm^2, respectively) for evoking ACh release from PPTg axons.

To record physiological events following local application of drugs, a drug-filled pipette was moved to within 20-40 μm of the recorded neuron using a second micromanipulator. A Picospritzer (General Valve) dispensed drug (dissolved in recording solution) onto the recorded neuron via a pressure ejection. Ejection volume, duration, and ejection pressure varied depending on the goal of the experiment. Approximate ejection pressures (in p.s.i.) for dispensing saturating ACh concentrations, ACh concentrations for testing galantamine potentiation, and PA-Nic application were 12, 2, and 2, respectively.

2-Photon Laser Scanning Microscopy, Electrophysiology, and Nicotine Uncaging - PA-Nic photolysis was performed as previously described (Banala et al., 2018). An Olympus BX51 upright microscope and a 60x (1.0 NA) objective was used to visualize cells. Prairie View 5.4 (Bruker Nano) software was used for image acquisition, photostimulation, and electrophysiology acquisition via a Multiclamp 700B patch clamp amplifier. Analog signals were sampled at 5 kHz and low-pass filtered at 1 kHz, and an A/D converter (PCI-NI6052e; National Instruments) was used for digitization. Patch clamp recordings were carried out using the internal solution mentioned above, except that Alexa 488 or 568 (100 μM) was also included in the recording pipette to visualize cells using 2-photon laser scanning microscopy. After break-in, the internal solution with the Alexa dye was allowed to equilibrate for 15-20 min before imaging was initiated. A Mai Tai HP1040 (Spectra Physics) was used to excite Alexa 488 or 568. Images in **Fig. 1b-d** were acquired by sequentially tuning and imaging, first at 920 nm to image Alexa 488 followed by 1040 nm to image tdT. Alexa 568 was used for cell imaging at 790 nm during uncaging experiments. The laser was pulsed at 90 MHz (~250 fs pulse duration), and a M350-80-02-BK Pockels cell (ConOptics) was used for power attenuation. The dual-channel, 2-photon fluorescence was detected by two non-de-scanned detectors; green and red channels (dual emission filters: 525/70 nm and 595/50 nm) were detected by the following Hamamatsu photomultiplier tubes (PMTs), respectively: end-on GaAsP (7422PA-40) and side-on multi-alkali (R3896). A 405 nm continuous wave laser (100 mW OBIS FP LX; Coherent) was used for photostimulation/uncaging via a second set of *x-y* galvanometers incorporated into the scanhead (Cambridge Technologies). 405 nm laser power was measured below the sample but above the condenser using a Field Master GS (LM10 HTD sensor head). PA-Nic (2 mM) was applied locally to the recorded cell via a large-bore (30-40 μm diameter) pressure ejection pipette at low pressure. The Markpoints module of Prairie View 5.4 software was used to select spots in the field of view (~1 μm diameter) for focal uncaging of nicotine via 405 nm laser light flashes (50 ms, 1-2 mW).

Supplemental References

Azam, L., Maskos, U., Changeux, J.P., Dowell, C.D., Christensen, S., De Biasi, M., and McIntosh, J.M. (2010). α-Conotoxin BuIA[T5A;P6O]: a novel ligand that discriminates between α6β4 and α6β2 nicotinic acetylcholine receptors and blocks nicotine-stimulated norepinephrine release. FASEB J *24*, 5113-5123.

Azam, L., Winzer-Serhan, U.H., Chen, Y., and Leslie, F.M. (2002). Expression of neuronal nicotinic acetylcholine receptor subunit mRNAs within midbrain dopamine neurons. J Comp Neurol *444*, 260-274.

Banala, S., Arvin, M.C., Bannon, N.M., Jin, X.T., Macklin, J.J., Wang, Y., Peng, C., Zhao, G., Marshall, J.J., Gee, K.R.*, et al.* (2018). Photoactivatable drugs for nicotinic optopharmacology. Nat Methods *15*, 347-350

Engle, S.E., Broderick, H.J., and Drenan, R.M. (2012). Local application of drugs to study nicotinic acetylcholine receptor function in mouse brain slices. J Vis Exp, e50034.

Mackey, E.D., Engle, S.E., Kim, M.R., O'Neill, H.C., Wageman, C.R., Patzlaff, N.E., Wang, Y., Grady, S.R., McIntosh, J.M., Marks, M.J.*, et al.* (2012). α6* Nicotinic Acetylcholine Receptor Expression and Function in a Visual Salience Circuit. J Neurosci *32*, 10226-10237.

Shih, P.Y., Engle, S.E., Oh, G., Deshpande, P., Puskar, N.L., Lester, H.A., and Drenan, R.M. (2014). Differential expression and function of nicotinic acetylcholine receptors in subdivisions of medial habenula. J Neurosci *34*, 9789-9802.

Wallace, M.L., Saunders, A., Huang, K.W., Philson, A.C., Goldman, M., Macosko, E.Z., McCarroll, S.A., and Sabatini, B.L. (2017). Genetically Distinct Parallel Pathways in the Entopeduncular Nucleus for Limbic and Sensorimotor Output of the Basal Ganglia. Neuron *94*, 138-152.

Xiao, L., Priest, M.F., Nasenbeny, J., Lu, T., and Kozorovitskiy, Y. (2017). Biased Oxytocinergic Modulation of Midbrain Dopamine Systems. Neuron *95*, 368-384.